Eur. Phys. J. E (2018) **41**: 135
DOI 10.1140/epje/i2018-11745-1

THE EUROPEAN PHYSICAL JOURNAL E

Regular Article

Transient electrohydrodynamics of a liquid drop in AC electric fields

A. Esmaeeli[a]

Southern Illinois University at Carbondale, 62901 Carbondale, IL, USA

Received 2 July 2018 and Received in final form 1 October 2018
Published online: 20 November 2018

Abstract. The transient behavior of a leaky dielectric liquid drop under a uniform AC electric field of small strength is investigated, using a closed form analytical solution. The drop settles to a quasi-steady state in a relaxation time that is set by the viscosities of the drop and the ambient fluid and the surface tension, and oscillates around a mean deformation with a frequency that is twice the electric field frequency. The mode of instantaneous deformation remains the same (oblate or prolate) or switches between oblate and prolate, depending on the relative importance of the time-periodic component of the deformation compared to that of the time-exponential. The structure of the flow field and its evolution is studied for representative fluid systems at a high and a low electric field frequency. The individual contribution of the net tangential and normal electric stresses, which are the driving forces of the problem, on the flow structure and drop deformation is characterized. On the basis of the mean (time-independent) and time-periodic components of the driving forces, the flow field is represented as the superposition of three different flow patterns. It is shown that the interplay of these flow patterns leads to formation and destruction of toroidal vortices, and that the residence time of these vortices correlates inversely with the field frequency.

1 Introduction

Interactions of electric field with liquid drops have been a problem of long-standing interest and is currently the focus of increased attention because of its relevance in a broad range of technologically advanced processes. Examples include break up of droplets in high electric fields for surface coating and spraying [1], enhancement of coalescence of droplets for de-emulsification purposes [2], and manipulation of droplets by electrowetting for digital microfluidic circuits [3], to name a few. The electric field modulates the phase boundary through interfacial electric stresses that arise due to mismatch of the dielectric properties of the fluids across the drop, leading to the drop deformation and fluid flow formation in and around it.

The theoretical foundation of the phenomenon was laid out by Taylor and Melcher [4–6] in a framework that later on became known as "Taylor-Melcher leaky dielectric theory" [7]. The essence of the model is to assume droplet fluid and the host fluid have finite electric conductivities and that the time scale of charge relaxation due to conduction from the fluid bulk to the drop surface to be much shorter than any process time of interest. The first assumption allows for the accumulation of free electric charges at the drop surface and, therefore, the possibility of interfacial electrical shear forces, which results in fluid flow at the drop surface even when the drop is stationary and its surface is immobile. The second assumption leads to substantial simplification of the mathematical formulation as the electric field equations will be decoupled from the momentum equation and reduce to quasi–steady-state laws.

The steady behavior of a drop in a DC electric field is reasonably well understood. Briefly, under a weak electric field the drop remains spherical or deforms to an ellipsoid whose major axis is in the direction of or perpendicular to the field, becoming a prolate or an oblate spheroid, respectively. Furthermore, a recirculatory flow in the form of toroidal vortices is established in and around the drop, where the external flow runs from the poles toward the equator or in the opposite direction. The key parameters that set the sense of drop deformation and fluid flow circulation are the electric conductivity ratio $\widetilde{\sigma} = \sigma_i/\sigma_o$ and the electric permittivity ratio $\widetilde{\epsilon} = \epsilon_i/\epsilon_o$ (drop fluid/host fluid). These parameters are asserted in the deformation characteristic function $\Phi(\widetilde{\sigma}, \widetilde{\epsilon}, \widetilde{\mu})$ ($\widetilde{\mu} = \mu_i/\mu_o$ being the viscosity ratio), and the interfacial tangential velocity u_{θ_i}, which are used to determine the senses of drop deformation and fluid flow circulation, respectively [8–10]. The expected shape of the drop and the flow pattern are typically

[a] e-mail: esmaeeli@engr.siu.edu

presented by the so-called deformation-circulation map (see fig. 2), which is constructed by plotting the zero-deformation curve $\Phi = 0$ and the zero-circulation line $u_{\theta_i} = 0$ together in a $\widetilde{\epsilon} - \widetilde{\sigma}$ coordinate.

While DC electric field provides a robust means for manipulation of the droplets, in many instances the use of an AC electric field proves to be more advantageous. For instance, in experimental studies to characterize the deformation of a stationary solitary drop, the drop will move toward one of the electrodes because of electrophoresis when it acquires a small net electric charge. The electrophoresis, however, can be eliminated in an AC field by adjusting the frequency [8]. Another advantage of an AC field is the possibility of changing the behavior of the fluid systems from leaky dielectric-leaky dielectric (LD-LD) to perfect dielectric-perfect dielectric (PD-PD) by adjusting the field frequency.

Despite the proven impact and potential applications of AC electric fields in manipulation of droplets, the number of studies in this regard are much more limited than those of the DC fields. In this paper, our focus is on the analytical solution of the problem. As such, we only refer to relevant studies in this context. Here the theoretical foundation of the problem was first laid out by Torza *et al.* [8], who considered a liquid drop, immersed in the pool of another liquid of infinite extension and exposed to an electric field strength of the form $\mathbf{E}_{ext}(t) = E_0\hat{\mathbf{k}}\cos\omega t$, $\hat{\mathbf{k}}$ being the unit vector in the field direction. The authors solved the axisymmetric creeping flow equations in conjunction with Laplace equation for the electric potential. In doing so, they ignored the convective term $\rho\mathbf{u}\cdot\nabla\mathbf{u}$ and the local acceleration term $\rho\partial\mathbf{u}/\partial t$ in the momentum equation. Thus, they were able to find a closed form analytical solution for the problem. For $\omega = 0$, the mean (time-independent) drop deformation $\mathcal{D}_m$ converged to that of Taylor's [4] steady-state solution $\mathcal{D}_m$ in a root-mean-square (*rms*) sense; *i.e.*, if the strength of the electric field in the DC field E_0 were replaced with $E_{rms} = E0/\sqrt{2}$ of the AC field. On the other hand, in the limit of $\omega \to \infty$, the mean deformation $\mathcal{D}_m$ converged to that of steady-state solution of Allan and Mason [11] concerning a perfect dielectric liquid drop in a perfect dielectric liquid (PD-PD) in a DC electric field, in an *rms* sense. This is conceivable, since at high frequency the time scale of charge migration from the fluids bulk to the surface ϵ/σ is much larger than the time scale of the change of the polarity of the electrodes $1/\omega$, and therefore, the fluid system behaves as a perfect dielectric. By inspection of the time-independent component of the interfacial electric shear stress $[\![\tau^e_{r\theta}]\!]_m$, the authors showed that the sense of the mean flow circulation around the drop is set by the sign of $\widetilde{\epsilon} - \widetilde{\sigma}$; *i.e.*, for fluid systems where $\widetilde{\epsilon} > \widetilde{\sigma}$, the mean flow will be from the equator to the poles, and the flow circulation will be in the opposite direction for fluid systems for which $\widetilde{\epsilon} < \widetilde{\sigma}$. The authors also determined the range of fluid property ratios $(\widetilde{\sigma}, \widetilde{\epsilon}, \widetilde{\mu})$ and frequencies (ω) for which the mean drop shape $\mathcal{D}_m$ would be oblate, prolate, or spherical, by examining the sign of the mean deformation characteristic function $\Phi_m = f(\widetilde{\sigma}, \widetilde{\epsilon}, \widetilde{\mu}; \omega)$. Accordingly, with respect to an AC electric field, they categorized the fluid systems to three different classes (or regions) on the basis of their senses of mean flow circulation and mean deformation.

Sozou [12] followed Torza, Cox, and Mason's study by improving their solution, accounting for the local acceleration term $\rho\partial\mathbf{u}/\partial t$ in the momentum equation. He showed that overlooking this term for fluids of low viscosity or fields of high frequency can lead to inaccurate results, qualitatively and quantitatively. In other words, the local acceleration term can be safely ignored only if $Re_\omega = \rho\omega a^2/\mu \ll 1$, where Re_ω is the Reynolds number based on the velocity scale $u_s = 2a\omega$, and a is the drop radius. Unfortunately, not much insight can be discerned from Sozou's study since the solution is not in a closed form and the results are pertained to two fluid systems only. Not many theoretical studies seem to have been performed about this problem in the intervening period between the publication of Sozou's work and the turn of the century. In recent years, however, there has been a resurgence of interest on the subject, driven mostly by its potential applications in microfluidics and biofluidics; see, for example, ref. [13], and the references therein.

The goal of this study is to explore the evolution of the flow field in and around a liquid drop under a uniform AC electric field of small strength, using a simple-closed form analytical solution. We are motivated by the fact that the electrohydrodynamic-driven flow finds relevance in a host of applications, such as enhancement of mixing by chaotic advection [14–17] and heat transfer enhancement by convection [18]. Surprisingly, with the exception of a recent numerical study by ref. [19] in the context of a two-dimensional drop, neither the structure of the flow field nor its evolution under an AC electric field has been studied so far, and this in turn, has led to some misconception. Ward and Homsy [14], for instance, in their experimental and theoretical study of enhancement of chaotic mixing considered the flow pattern inside the drop in an AC field to be the same as that in a steady-state DC field, with the only difference between the two being the strength of the flow field to be time-periodic in the former. This is, however, not true, as will be seen later in this study. Indeed, whereas the steady-state flow pattern in a liquid drop in a DC electric field comprises of four counter-rotating vortices (in the plane of symmetry), the flow pattern inside the drop in an AC electric field evolves continuously and at times comprises open-ended streamlines that cross the drop. To this end, we build on Torza *et al.* solution [8] and solve creeping flow equations, ignoring the convective and the acceleration terms. However, there are two main differences between our work and that of those authors. First, we account for the transient evolution of the flow field toward the time-periodic state. As will be shown in the result section, the transient time can be rather long for some choices of input parameters. Second, these authors derived the solution as a superposition of the flow driven by the electric shear stress and that due to the electric normal stress, and while their overall solution is correct, this is not the case for the two superimposed solutions. This issue is rectified here and discussed. We also provide a formalism for this problem using scaling arguments,

which show how the simplified equations are related to the original ones. Torza *et al.*, on the other hand, explored the validity of their results *posteriorly* by comparison of the magnitude of the terms that they ignored at the outset with those that they retained, using their solution. The closed form analytical solution presented here, will provide a theoretical basis for the interpretation of the numerical and experimental results of the problem.

The organization of the paper is as follows. In sect. 2 we discuss the problem statement, including the governing equations. In sects. 3, 4 the solution of the electric field and momentum equations are presented. Sections 5–7 deal, respectively, with the construction of the deformation-circulation map, the summary of our solution, and the difference between our solution and that of Torza *et al.* [8]. Section 8 contains the results, in which we explore the general features of the problem in terms of the deformation and fluid flow. In sect. 9 we discuss the relevance of the results to microfluidic applications. Finally in sect. 10 we conclude with a discussion of the new findings.

2 Problem formulation

The definition sketch of the problem is shown in fig. 1, depicting a liquid drop of radius a suspended in another liquid, and exposed to a uniform alternating electric field far away from the drop

$$\mathbf{E}_{ext} = \mathbf{E}_0 \cos \omega t, \tag{1}$$

where $\omega = 2\pi\nu$ is the angular field frequency [rad/s], and ν is the ordinary frequency [Hz]. The fluids are incompressible, immiscible, and Newtonian, and the governing equations of the problem are mass and momentum conservation equations and the electric field equations.

We use Taylor-Melcher leaky dielectric model to account for the electrohydrodynamic force in the momentum equation. In this model, the fluids are assumed to have finite electric conductivity in order to allow for accumulation of free electric charge at the interface. The action of the electric field on the surface charge leads to interfacial normal and tangential electric stresses. The formalism of the leaky dielectric model was introduced by Taylor and Melcher [5,6,20], but it was brought to perfection by Saville [7] through the use of electrokinetic equations and scaling arguments. Briefly, using scaling arguments, Saville asserted that in the absence of an external magnetic filed the magnetic effect can be ignored completely at a millimeter length scale, since the characteristic time of the electrostatic phenomenon $\tau_C = \epsilon/\sigma$ is much larger than that of the magnetic phenomenon $\tau_M = \mu\sigma\ell^2$; ϵ, σ, and μ being, respectively, the electric permittivity, the electric conductivity, and the magnetic permeability. Thus, the Faraday's law $\partial\mathbf{B}/\partial t + \nabla \times \mathbf{E} = 0$ can be simplified to $\nabla \times \mathbf{E} = 0$, which suggests $\mathbf{E} = -\nabla\phi$, where ϕ is the electric potential. He further showed that at a millimeter length scale ($\ell = 10^{-3}$ m) the fluids are electrically neutral (*i.e.*, no free electric charge in the bulk) by considering the equation of conservation of volume charge q_v in nondimensional

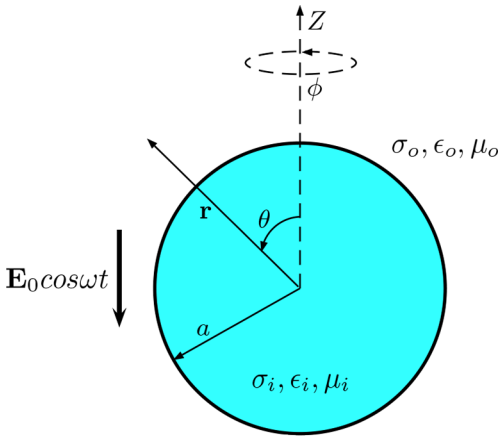

Fig. 1. The problem setup, depicting a liquid drop in a pool of another liquid.

form, in terms of the concentration of anions, cations, and neutral species, and properties of a common liquid ($\rho = 10^3\,\mathrm{kg/m^3}$, $\mu = 1\,\mathrm{Pa \cdot s}$, $\sigma = 10^{-9}\,\mathrm{S/m}$, $\epsilon = 4\epsilon_0\,\mathrm{F/m}$) in an electric field strength of $E_0 = 10^5\,\mathrm{V/m}$. Assuming further that the convective effects are weak, the (volume) charge conservation equation is simplified to $\nabla \cdot \sigma\mathbf{E} = 0$, or in terms of electric potential $\nabla \cdot \sigma\nabla\phi = 0$, where for uniform electric conductivity this equation can be written as

$$\nabla^2 \phi_{i,o}(r, \theta, t) = 0 \tag{2}$$

for the fluids inside and outside,

$$\nabla^2 = \frac{1}{r^2}\frac{\partial}{\partial r}\left(r^2 \frac{\partial}{\partial r}\right) + \frac{1}{r^2 \sin\theta}\frac{\partial}{\partial \theta}\left(\sin\theta \frac{\partial}{\partial \theta}\right)$$

being the Laplacian in spherical coordinates.

Equation (2) should be supplemented by the conservation of surface charge q_s equation. Torza *et al.* [8] used the following equation:

$$\frac{\partial q_s}{\partial t} - \left[\!\left[\sigma \frac{\partial \phi}{\partial n}\right]\!\right] = 0 \tag{3}$$

at the outset and then evaluated the range of its applicability posteriorly by evaluation of the terms that they eliminated from the original equation, using their solution. Here the double bracket denotes jump in the quantity inside the bracket across the interface (outside minus inside). To explore the conditions under which the surface charge conservation equation can be simplified, we start with the most general form of this equation [21]

$$\frac{\partial q_s}{\partial t} + u_n \nabla \cdot (q_s \mathbf{n}) + \nabla_s \cdot (\sigma_f \mathbf{E}_s + \mathbf{u}_s q_s) - \left[\!\left[\sigma \frac{\partial \phi}{\partial n}\right]\!\right] = 0, \tag{4}$$

where u_n and $\mathbf{u}_s$ are the normal and the tangential components of the velocity field at the drop surface, $\mathbf{E}_s$ is the electric field strength at the drop surface, $\nabla_s = \nabla - \mathbf{nn} \cdot \nabla$ is the surface divergence, σ_f is the surface conductance, and $\partial/\partial n = \mathbf{n} \cdot \nabla$. Here $\mathbf{n}$ is a unit vector normal to the

drop surface. Nondimensionalization of eq. (4), using the following scales:

$$l_{sc} = a,\ u_{sc} = \frac{\epsilon_o E_0^2 a}{\mu_o} \equiv u_h, \tag{5a}$$

$$t_{sc} = \tau_P,\ q_{sc} = \epsilon_o E_0,\ \phi_{sc} = E_0 a,\ \sigma_{sc} = \sigma_o,\ \sigma_{f_{sc}}, \tag{5b}$$

as the scales of length, velocity, time, surface charge, electric potential, conductivity, and surface conductance, respectively, leads to

$$\frac{\tau_C}{\tau_P}\frac{\partial q_s^*}{\partial t^*} + \frac{\tau_C}{\tau_F}\left[u_n^* \nabla^* \cdot (q_s^* \mathbf{n}) + \nabla_s^* \cdot (\mathbf{u}_s^* q_s^*)\right] + \frac{\sigma_{f_{sc}}}{\sigma_o a}\nabla_s^* \cdot (\sigma_{f_s}^* \mathbf{E}_s^*) - \left[\frac{\partial \phi_o^*}{\partial n^*} - \sigma^* \frac{\partial \phi_i^*}{\partial n^*}\right] = 0. \tag{6}$$

In eq. (6), $\sigma^* = \sigma_i/\sigma_o$ is the conductivity ratio, $\tau_C = \epsilon_o/\sigma_o$ is the time scale of charge relaxation from the bulk to the fluid interface, $\tau_F = a/u_h$ is the time scale of charge convection, and τ_P is the process time of the interest. τ_P can be considered as the time scale of electric field oscillation $\tau_P = 1/\omega$ or the time scale of drop deformation $\tau_P = \mu_o a/\gamma$, in which the drop relaxes to its mean (time-independent) deformation. Thus, $\tau_C/\tau_P = \{\Pi = \epsilon_o\omega/\sigma_o,\ Sa = \epsilon_o\gamma/\sigma_o\mu_o a\}$, Π and Sa being the Pi and Saville numbers, respectively. The first choice, $\tau_C/\tau_P = \Pi$, is relevant for evaluation of eq. (6) in the quasi-steady state (time-periodic stage), while the second choice, $\tau_C/\tau_P = Sa$ is relevant for the transient stage, which precedes the time-periodic stage. As can be inferred from eq. (6), the last bracket should be always accounted for. The contribution of the first term should be taken into account if $\tau_C/\tau_P \equiv \{\Pi, Sa\}$ is not too large or too small. If $\Pi \ll 1$ or $Sa \ll 1$, the first term can be ignored. On the other hand, if $\Pi \gg 1$ or $Sa \gg 1$, only the first term will survive, suggesting that the fluid system behaves as a perfect dielectric system. The first bracket couples the electric field equation to the fluid flow equation. For creeping flows, this term can be easily ignored, since $\tau_C/\tau_F \ll 1$ represents the ratio of the time scale of charge relaxation to the time scale of charge convection. This ratio is called the electric Reynolds number, $Re_{el} = \epsilon_o u_h/\sigma_o a$. The fourth term does not lead to a coupling of the electric field and fluid flow equations. However, it can make the analytical derivations more tedious. Furthermore, not much information seems to be available regarding the magnitude of the surface conductance σ_f. This term can be ignored if $\sigma_{f_{sc}}/\sigma_o a \ll 1$. In summary, assuming

$$\frac{\tau_C}{\tau_P} = \frac{\epsilon_o\omega}{\sigma_o} \equiv \Pi = O(1), \qquad \frac{\tau_C}{\tau_P} = \frac{\epsilon_o\gamma}{\mu_o a\sigma_o} \equiv Sa = O(1),$$
$$\frac{\tau_C}{\tau_F} = \frac{\epsilon_o u_h}{\sigma_o a} \equiv Re_{el} \ll 1, \qquad \frac{\sigma_{f_{sc}}}{\sigma_o a} \ll 1, \tag{7}$$

leads to eq. (3).

In passing it is worth mentioning that Torza *et al.* in their posteriori analysis of the effect of the surface conductance (which appears in eq. (4)) pointed out that accounting for this term would lead to an increase of the algebraic value of the (surface) charges facing the negative electrode and a decrease of those facing the positive electrode. Hence, it would lead to an increase in the mean deformation $\mathcal{D}_m$. Accordingly, they concluded that the effect of the surface conductance was analogous to that of increasing the conductivity of the drop. The authors did not comment on the effect of the charge convection on the results. However, Feng [22], who studied this effect in the context of DC electric fields, showed that the main effect of charge convection is to reduce the interfacial velocity, leading to oblate drops to deform less but prolate drops to deform more. We believe a similar comment can be made regarding the mean deformation of a drop in AC fields.

The momentum equation for both fluids is

$$\rho\left(\frac{\partial \mathbf{u}}{\partial t} + \mathbf{u}\cdot\nabla\mathbf{u}\right) = -\nabla p + \mu\nabla^2\mathbf{u}, \tag{8}$$

where the electrohydrodynamic (EHD) force does not appear in this equation because it is confined to the interface. Nondimensionalization of eq. (8), considering $l_s = a$, $t_s = \tau_P$, $u_s = u_h$, $p_s = \epsilon_o E_0^2$ as scales of the length, time, velocity, and pressure, leads to

$$\frac{\tau_{diff}}{\tau_P}\rho^*\frac{\partial \mathbf{u}^*}{\partial t^*} + Re_f \mathbf{u}^*\cdot\nabla^*\mathbf{u}^* = -\nabla^* p^* + \mu^*\nabla^{*2}\mathbf{u}^*. \tag{9}$$

Here $\rho^* = \rho_i/\rho_o$, $\mu^* = \mu_i/\mu_o$ in the inside and $\rho^* = 1$, $\mu^* = 1$ in the outside. $\tau_{diff} = a^2/\nu_o$ is the time scale of momentum diffusion, where $\nu_o = \mu_o/\rho_o$, and $Re_f = \rho_o a u_h/\mu_o$ is the fluid Reynolds number. Again, considering the process time of interest to be the time scale of electric field oscillation $\tau_P = 1/\omega$ or the time scale of drop deformation $\tau_P = \mu_o a/\gamma$ leads to $\tau_{diff}/\tau_P \equiv Re_\omega = a^2\omega/\nu_o$ or $\tau_{diff}/\tau_P \equiv Oh^{-2} = \rho_o\gamma a/\mu_o^2$, respectively, where Re_ω is the Reynolds number based on the electric field velocity scale and Oh is the Ohnesorge number. Assuming $\tau_{diff}/\tau_P \ll 1$, the first term can be ignored, provided $\rho_i/\rho_o = O(1)$. For creeping flows, $Re_f = \rho_o u_s a/\mu_o \ll 1$, and thus, the second term can be also ignored, leading to

$$-\nabla p + \mu\nabla^2\mathbf{u} = 0, \tag{10}$$

provided $\mu_i/\mu_o = O(1)$. Equation (10), in conjunction with the mass conservation equation ($\nabla\cdot\mathbf{u} = 0$), yields

$$D^4\psi_{i,o} = 0, \tag{11}$$

where ψ in the streamfunction, which is related to the velocity field by

$$u_r = \frac{1}{r^2\sin\theta}\frac{\partial\psi}{\partial\theta}, \qquad u_\theta = -\frac{1}{r\sin\theta}\frac{\partial\psi}{\partial r},$$

$D^4 = D^2(D^2)$, where

$$D^2 = \frac{\partial^2}{\partial r^2} + \frac{\sin\theta}{r^2}\frac{\partial}{\partial\theta}\left(\frac{1}{\sin\theta}\frac{\partial}{\partial\theta}\right)$$

resembles the Laplacian.

In addition to the nondimensional numbers considered so far, the capillary numbers based on the electrohydrodynamic velocity scale $Ca_f = \mu_o u_h/\gamma$ and the oscillatory

hydrodynamic stress $Ca_\omega = \mu_o u_\omega/\gamma$, where $u_\omega = a\omega$, also come to the picture. For the problem at hand, where we assume that the interface remains nearly spherical, the fluid flow-based capillary number should be small, $Ca_f \ll 1$. However, no restriction needs to be imposed on the electric-based capillary number Ca_ω. In summary, the governing nondimensional parameters of the problem, without any restrictions, are

$$Ca_\omega = \frac{\mu_o \omega a}{\gamma}, \quad \Pi = \frac{\epsilon_o \omega}{\sigma_o}, \quad \widetilde{\sigma} = \frac{\sigma_i}{\sigma_o}, \quad \widetilde{\epsilon} = \frac{\epsilon_i}{\epsilon_o}, \quad (12)$$

while

$$Ca_f = \frac{\mu_o u_h}{\gamma} \ll 1,\ Re_f = \frac{\rho_o a u_h}{\mu_o} \ll 1,\ Re_{el} = \frac{\epsilon_o u_h}{\sigma_o a} \ll 1, \quad (13a)$$

$$Oh^2 = \frac{\mu_o^2}{\rho_o a \gamma} \gg 1, \quad Re_\omega = \frac{a^2\omega}{\nu_o} \ll 1, \quad (13b)$$

$$\frac{\sigma_{f_{sc}}}{\sigma_o a} \ll 1, \quad \widetilde{\mu} = \frac{\mu_i}{\mu_o} = O(1), \quad \widetilde{\rho} = \frac{\rho_i}{\rho_o} = O(1) \quad (13c)$$

are the nondimensional numbers that have some restrictions. Notice that Π is considered without a restriction since in the limit of $\Pi \ll 1$ the solution converges to that corresponding to a steady-state DC field, while for $\Pi \gg 1$ the fluid system behaves as perfect dielectric.

3 Solution of the electric potential equation

To find the electric potential fields inside and outside of the drop, eq. (2) should be solved subject to the following boundary and jump conditions:

i) The electric field strength far away from the drop converges to the unperturbed external field $\mathbf{E}_{ext}$. This translates to $\phi_o(\infty, \theta, t) \sim E_0 r \cos\theta \cos\omega t$, in terms of ϕ.
ii) The electric potential inside the drop should remain finite; $\phi_i(0, \theta, t)$ should be bounded.
iii) The jump in the normal (radial) component of the electric displacement $D_r = \epsilon E_r$ at the drop surface is equal to the surface charge density; $q_s = \epsilon_o E_{r_o} - \epsilon_i E_{r_i}$, or in terms of ϕ, $q_s = \epsilon_i \partial\phi_i/\partial r - \epsilon_o \partial\phi_o/\partial r$.
iv) Continuity of the electric potential at the drop surface, $\phi_i(a, \theta, t) = \phi_o(a, \theta, t)$.
v) Conservation of the surface charge, eq. (3).

Since eq. (2) and its boundary and jump conditions are linear, we use "the method of complex variables", by seeking the solution of $\nabla^2\phi' = 0$, where $\phi'(r, \theta, t) = \phi^*(r, \theta)e^{i\omega t}$ is a complex potential whose real part $\phi = \mathbb{R}\mathrm{e}(\phi')$ constitutes the solution, ϕ^* being the time-independent complex potential. Similarly, we consider $\mathbf{E}_{exe} = \mathbb{R}\mathrm{e}(\mathbf{E}'_{exe})$, where $\mathbf{E}'_{exe} = \mathbf{E}_0 e^{i\omega t}$, and $q_s = \mathbb{R}\mathrm{e}(q'_s)$, where $q'_s(r, \theta, t) = q^*_s(r, \theta)e^{i\omega t}$. Accordingly, eq. (2) will be converted to $\nabla^2\phi^*_{i,o} = 0$, and the boundary and jump conditions will be in terms of the complex potentials, ϕ^*_i and ϕ^*_o. Once the solutions of ϕ^*_i and ϕ^*_o are found, the electric potentials inside and outside are determined to be

$$\phi_i = 3E_0 r \cos\theta\, \mathbb{R}\mathrm{e}(A^* e^{i\omega t}), \quad (14a)$$

$$\phi_o = E_0 r \cos\theta\, \mathbb{R}\mathrm{e}\left\{\left[1 + (3A^* - 1)\left(\frac{a}{r}\right)^3\right] e^{i\omega t}\right\}, \quad (14b)$$

where

$$A^* = \frac{1 + i\Pi}{(\widetilde{\sigma} + 2) + i\Pi(\widetilde{\epsilon} + 2)}. \quad (15)$$

The electric field can be readily found from $\mathbf{E} = -\nabla\phi$, leading to

$$\mathbf{E}_i = 3\mathbf{E}_0 \frac{\sqrt{a_i^2 + b_i^2}}{\Lambda} \cos(\omega t - \alpha_{E_i}), \quad (16a)$$

$$a_i = (\widetilde{\sigma} + 2) + \Pi^2(\widetilde{\epsilon} + 2), \qquad b_i = \Pi(\widetilde{\epsilon} - \widetilde{\sigma}),$$

$$\alpha_{E_i} = \tan^{-1}\left(\frac{b_i}{a_i}\right), \quad (16b)$$

$$\Lambda = (\widetilde{\sigma} + 2)^2 + \Pi^2(\widetilde{\epsilon} + 2)^2, \quad (16c)$$

and

$$\mathbf{E}_o = \mathbf{E}_{ext} - \frac{\sqrt{a_o^2 + b_o^2}}{\Lambda}\left[\mathbf{E}_0\left(\frac{a}{r}\right)^3 - \frac{3(\mathbf{E}_0 \cdot \mathbf{r})\mathbf{r}a^3}{r^5}\right] \times \cos(\omega t - \alpha_{E_o}), \quad (17a)$$

$$a_o = (\widetilde{\sigma}^2 + \widetilde{\sigma} - 2) - \Pi^2(\widetilde{\epsilon}^2 + \widetilde{\epsilon} - 2),$$

$$b_o = 3\Pi(\widetilde{\sigma} - \widetilde{\epsilon}), \qquad \alpha_{E_o} = \tan^{-1}\left(\frac{b_o}{a_o}\right). \quad (17b)$$

The electric field inside the drop $\mathbf{E}_i$ is uniform and has a phase lag of α_{E_i} with respect to the imposed electric field $\mathbf{E}_{ext}$. Equation (17) suggests that the electric field in the ambient $\mathbf{E}_o$ comprises of the imposed electric field $\mathbf{E}_{ext}$ and an electric dipole at the center of the drop whose dipole moment will be colinear with or anti-parallel to the external field, depending on the interplay of the conductivity and permittivity ratios and the instantaneous direction of $\mathbf{E}_{ext}$.

3.1 Free electric charge at the interface

The free surface charge at the interface is found from $q_s = (\epsilon_i \partial\phi_i/\partial r - \epsilon_o \partial\phi_o/\partial r)|_{r=a}$, using eq. (14). This yields

$$q_s = \frac{3\epsilon_o E_0(\widetilde{\epsilon} - \widetilde{\sigma})}{\sqrt{\Lambda}} \cos\theta \cos(\omega t - \alpha_q), \quad (18a)$$

$$\alpha_q = \tan^{-1}\left(\frac{\Pi(\widetilde{\epsilon} + 2)}{\widetilde{\sigma} + 2}\right); \qquad 0 \le \alpha_q \le \pi/2, \quad (18b)$$

Equation (18) suggests that the distribution of the free charge on the interface depends on the amplitude of the unperturbed electric field E_0 and the relative magnitude of $\widetilde{\sigma}$ and $\widetilde{\epsilon}$. Furthermore, the net free surface charge at a given time is zero, $\int q_s \mathrm{d}A = 0$, A being the surface of the drop. Compared to the applied external field, the charge has a time lag. For $\omega(\Pi) = 0$, eq. (18) converges to that for a uniform DC electric field [23]. For $\omega(\Pi) \to \infty$, $q_s = 0$, since the fluid system behaves as a perfect dielectric.

3.2 The net interfacial electric stresses

The interfacial tangential and normal electric stresses are the drivers behind the fluid flow circulation and interface deformation, respectively. To calculate these terms, the electric stresses must be evaluated first using the Maxwell stress tensor, $\boldsymbol{\tau}_M = \epsilon\mathbf{EE} - (1/2)\epsilon\mathbf{E}\cdot\mathbf{EI}$. Accordingly, the jump in the normal and tangential electric stresses are

$$[\![\tau^e_{rr}]\!] = \frac{1}{2}\epsilon_o\left[E^2_{r_o} - \widetilde{\epsilon}E^2_{r_i} - (1-\widetilde{\epsilon})E^2_\theta\right], \tag{19a}$$

$$[\![\tau^e_{r\theta}]\!] = \epsilon_o E_\theta\left(E_{r_o} - \widetilde{\epsilon}E_{r_i}\right), \tag{19b}$$

where $E_{\theta_i} = E_{\theta_o} \equiv E_\theta$, and for a physical parameter such as Q, the jump is defined as

$$[\![Q]\!] = Q_o - Q_i. \tag{20}$$

The net interfacial electric stresses will comprise a mean (time-independent) and a time-periodic component

$$[\![\tau^e_{rr}]\!] = [\![\tau^e_{rr}]\!]_m + [\![\tau^e_{rr}]\!]_{tp}, \tag{21a}$$

$$[\![\tau^e_{r\theta}]\!] = [\![\tau^e_{r\theta}]\!]_m + [\![\tau^e_{r\theta}]\!]_{tp}. \tag{21b}$$

Identification of these components will facilitate the analysis of the problem. To proceed, we use eq. (14) and $\mathbf{E}_{i,o} = -\nabla\phi_{i,o}$ to evaluate the electric field at the interface, leading to

$$E_{r_i} = -3E_0\cos\theta\,\mathbb{R}\mathrm{e}(A^*e^{i\omega t}), \tag{22a}$$

$$E_{\theta_i} = E_{\theta_o} \equiv E_\theta = 3E_0\sin\theta\,\mathbb{R}\mathrm{e}(A^*e^{i\omega t}), \tag{22b}$$

$$E_{r_o} = 3E_0\cos\theta\,\mathbb{R}\mathrm{e}[(2A^*-1)e^{i\omega t}]. \tag{22c}$$

Substitution for E_r and E_θ from eq. (22) in eq. (19) results in the net normal electric stress (it is also called the electric pressure)

$$[\![\tau^e_{rr}]\!]_m = \frac{9\epsilon_o E_0^2}{4\Lambda}\left\{\left[(\widetilde{\sigma}^2 - 2\widetilde{\epsilon}+1) + \Pi^2(\widetilde{\epsilon}-1)^2\right]\cos^2\theta + \left[(\widetilde{\epsilon}-1)(\Pi^2+1)\right]\right\}, \tag{23a}$$

$$[\![\tau^e_{rr}]\!]_{tp} = \frac{9\epsilon_o E_0^2}{4}\mathbb{R}\mathrm{e}(F_r^*e^{2i\omega t})\cos^2\theta + \frac{9\epsilon_o E_0^2}{8}(\widetilde{\epsilon}-1) \times\left[A^{*2}e^{2i\omega t} + \bar{A}^{*2}e^{-2i\omega t}\right], \tag{23b}$$

and the net tangential electric stress

$$[\![\tau^e_{r\theta}]\!]_m = \frac{9\epsilon_o E_0^2(\widetilde{\epsilon}-\widetilde{\sigma})}{4\Lambda}\sin 2\theta, \tag{24a}$$

$$[\![\tau^e_{r\theta}]\!]_{tp} = \frac{9\epsilon_o E_0^2(\widetilde{\epsilon}-\widetilde{\sigma})}{4}\mathbb{R}\mathrm{e}(F_\theta^*e^{2i\omega t})\sin 2\theta, \tag{24b}$$

where

$$F_r^* = A^{*2}(5-2\widetilde{\epsilon}) - 4A^* + 1, \tag{25a}$$

$$F_\theta^* = \frac{1+i\Pi}{[(\widetilde{\sigma}+2)+i\Pi(\widetilde{\epsilon}+2)]^2}. \tag{25b}$$

In passing, it is to be noted that Torza *et al.* [8] reported $F_r^* = A^{*2}(5-2\widetilde{\epsilon}) - 2A^* + 1$, due to a typographical error.

4 Solution of the momentum equation

Since the net normal and tangential electric stresses, which are the driving forces of this problem, comprises mean and time-periodic components, the streamfunction $\psi(r,\theta,t)$ will have a time-exponential ψ^{te} (see ref. [24]) and a time-periodic ψ^{tp} component, respectively. To facilitate the analysis of the results, it will be beneficial to decompose the solution based on these components. The time-periodic solution, however, can be further decomposed in terms of the tangential and normal electric stresses; $\psi^{tp} = \psi^{tp}_T + \psi^{tp}_N$. Accordingly, we consider a solution of the form

$$\psi_i = \psi^{te}_i + \psi^{tp}_{i_T} + \psi^{tp}_{i_N}, \tag{26a}$$

$$\psi_o = \psi^{te}_o + \psi^{tp}_{o_T} + \psi^{tp}_{o_N}, \tag{26b}$$

for the streamfunction, and of the form

$$\mathbf{u}_i = \mathbf{u}^{te}_i + \mathbf{u}^{tp}_{i_T} + \mathbf{u}^{tp}_{i_N}, \tag{27a}$$

$$\mathbf{u}_o = \mathbf{u}^{te}_o + \mathbf{u}^{tp}_{o_T} + \mathbf{u}^{tp}_{o_N}, \tag{27b}$$

for the velocity field. Similarly, the jumps in the hydrodynamic stresses and pressure, which come into the picture in the momentum jump conditions, are written as

$$[\![\mathcal{S}]\!] = [\![\mathcal{S}]\!]_{te} + [\![\mathcal{S}]\!]^T_{tp} + [\![\mathcal{S}]\!]^N_{tp}, \tag{28}$$

where $\mathcal{S} = \{\tau^h_{rr}, \tau^h_{r\theta}, p\}$. Note that $[\![\mathcal{S}]\!]_{te}$ is due to the mean net electric stresses, $[\![\tau^e_{rr}]\!]_m$ and $[\![\tau^e_{r\theta}]\!]_m$, while $[\![\mathcal{S}]\!]^T_{tp}$ and $[\![\mathcal{S}]\!]^N_{tp}$ are due to time-periodic net shear and normal electric stresses, $[\![\tau^e_{r\theta}]\!]_{tp}$ and $[\![\tau^e_{rr}]\!]_{tp}$, respectively.

The formal solution of the streamfunction ψ, accounting for the fact that the velocity field inside the drop should be finite and that it will diminish far away from the drop, reads

$$\psi_i = (A_i r^3 + B_i r^5)\sin^2\theta\cos\theta, \tag{29a}$$

$$\psi_o = (A_o r^{-2} + B_o)\sin^2\theta\cos\theta, \tag{29b}$$

where $A_{i,o}(t)$ and $B_{i,o}(t)$ are four unknown coefficients that are determined by the interfacial jump condition. In the course of the solution, we also need to account for the drop deformation. For slightly deformed drops, the deformation is typically defined as $\mathcal{D} = (z_{max} - r_{max})/(z_{max} + r_{max})$, where z_{max} and r_{max} are the end-to-end length of the drop in the direction of electric field and the maximum breadth in the transverse direction, respectively. In a manner similar to the decomposition of the streamfunction, the total deformation is written as

$$\mathcal{D} = \mathcal{D}_{te} + \mathcal{D}^T_{tp} + \mathcal{D}^N_{tp}, \tag{30}$$

where $\mathcal{D}_{te}$ is the time-exponential component of the deformation, which is due to $[\![\tau^e_{rr}]\!]_m$ and $[\![\tau^e_{r\theta}]\!]_m$, $\mathcal{D}^T_{tp}$ is due to $[\![\tau^e_{r\theta}]\!]_{tp}$, and $\mathcal{D}^{tp}_N$ is due to $[\![\tau^e_{rr}]\!]_{tp}$.

4.1 Fluid flow and drop deformation due to the mean net normal and tangential electric stresses, $[\![\tau^{e}_{rr}]\!]_{m}$ and $[\![\tau^{e}_{r\theta}]\!]_{m}$

The detail of the solution is given in appendix A. Here the streamfunction is

$$\psi_i^{te} = \left\{ a^2 U_m \left[\left(\frac{r}{a}\right)^3 - \left(\frac{r}{a}\right)^5 \right] + a^2 U_{te} \Big[(16\widetilde{\mu}+19) \left(\frac{r}{a}\right)^3 - 3(2\widetilde{\mu}+3) \left(\frac{r}{a}\right)^5 \Big] \right\} \sin^2\theta\cos\theta, \tag{31a}$$

$$\psi_o^{te} = \left\{ a^2 U_m \left[\left(\frac{a}{r}\right)^2 - 1 \right] + a^2 U_{te} \Big[-3(3\widetilde{\mu}+2) \left(\frac{a}{r}\right)^2 + (19\widetilde{\mu}+16) \Big] \right\} \sin^2\theta\cos\theta, \tag{31b}$$

where

$$U_m = \frac{9u_h(\widetilde{\epsilon}-\widetilde{\sigma})}{20(\widetilde{\mu}+1)\Lambda} \tag{32}$$

is the maximum velocity in the mean flow (*i.e.*, $t \to \infty$), $u_h = \epsilon_o E_0^2 a/\mu_o$ being the electrohydrodynamic velocity scale, and

$$U_{te} = \frac{3}{4}\frac{u_h}{(19\widetilde{\mu}+16)(2\widetilde{\mu}+3)} \Phi_m \exp\left(-\frac{t}{\tau}\right) \tag{33}$$

is the maximum time-exponential velocity. As is evident, eq. (31) consists of two parts; a mean (time-independent) part (the first bracket), and a transient time-exponentially decaying part (the second bracket). For $\omega = 0$ and $t \to \infty$, eq. (31) converges to that of Taylor's solution for a drop in a DC electric field.

The time-exponential drop deformation is

$$\mathcal{D}_{te} = \mathcal{D}_m \left[1 - \exp(-t/\tau)\right], \tag{34}$$

where

$$\mathcal{D}_m = \frac{9}{32} Ca_f \Phi_m, \tag{35a}$$

$$\Phi_m = 1 - \frac{15(\widetilde{\mu}+1) + \widetilde{\sigma}(11\widetilde{\mu}+14)}{5(\widetilde{\mu}+1)\Lambda} - \frac{\widetilde{\epsilon}(19\widetilde{\mu}+16) + 15\Pi^2(\widetilde{\mu}+1)(2\widetilde{\epsilon}+1)}{5(\widetilde{\mu}+1)\Lambda}, \tag{35b}$$

$$\tau = \frac{a\mu_o}{\gamma}\frac{(19\widetilde{\mu}+16)(2\widetilde{\mu}+3)}{40(\widetilde{\mu}+1)}. \tag{35c}$$

In eq. (35), $\mathcal{D}_m$ is the mean (time-independent) deformation (*i.e.*, $t \to \infty$), Φ_m is the associated deformation characteristic function, and τ is the relaxation time toward the mean deformation. Φ_m determines the sense of mean drop deformation; for $\Phi_m > 0$ the drop elongate in the direction of the field, becoming a prolate, for $\Phi_m < 0$ it elongates in the direction perpendicular to the field, becoming an oblate, and for $\Phi_m = 0$ it remains spherical. We note that the relaxation time τ here is the same as that for a drop in a DC electric field under $Oh^2 \gg 1$ and $Ca_f \ll 1$, per ref. [24].

For comparison, we also report the drop deformation in a steady-state DC electric field for a leaky dielectric fluid system

$$\mathcal{D}_0 = \frac{9}{16} Ca_f \Phi_0, \tag{36a}$$

$$\Phi_0 = \frac{1}{(\widetilde{\sigma}+2)^2}\left(\widetilde{\sigma}^2 + 1 - 2\widetilde{\epsilon} + \frac{3}{5}\frac{3\widetilde{\mu}+2}{\widetilde{\mu}+1}(\widetilde{\sigma}-\widetilde{\epsilon})\right), \tag{36b}$$

and a perfect dielectric (PD) fluid system

$$\mathcal{D}_{0_{PD}} = \frac{9}{16} Ca_f \Phi_{0_{PD}}, \tag{37a}$$

$$\Phi_{0_{PD}} = \left(\frac{\widetilde{\epsilon}-2}{\widetilde{\epsilon}+2}\right)^2. \tag{37b}$$

For $\omega = 0$, $\Phi_m = \Phi_0$ and the mean deformation $\mathcal{D}_m$ will be the same as the deformation in the DC electric field $\mathcal{D}_0$ for leaky dielectric fluid systems, provided $E_{rms} = E_0/\sqrt{2}$ is used in lieu of E_0 in calculation of $Ca_f = \epsilon_o E_0^2 a/\gamma$ in the DC electric field. Similarly, for $\omega \to \infty$, $\Phi_m = \Phi_{0_{PD}}$ and the mean deformation $\mathcal{D}_m$ will be the same as the deformation in the DC electric field $\mathcal{D}_{0_{PD}}$ for a perfect dielectric system, provided $E_{rms} = E_0/\sqrt{2}$ is used in lieu of E_0 in calculation of $Ca_f = \epsilon_o E_0^2 a/\gamma$ in the DC electric field.

4.2 Fluid flow and drop deformation due to the time-periodic net tangential electric stress, $[\![\tau^{e}_{r\theta}]\!]_{tp}$

We refer to the drop deformation and the velocity field due to $[\![\tau^{e}_{r\theta}]\!]_{tp}$ as the shear stress-driven deformation and flow, respectively. The detail of the solution is given in appendix B. Here the streamfunction is

$$\psi_{i_T}^{tp} = \left\{ a^2 U_{T_1}^{tp} \left[\left(\frac{r}{a}\right)^3 - \left(\frac{r}{a}\right)^5 \right] + a^2 U_{T_2}^{tp} \Big[(16\widetilde{\mu}+19) \left(\frac{r}{a}\right)^3 - 3(2\widetilde{\mu}+3) \left(\frac{r}{a}\right)^5 \Big] \right\} \sin^2\theta\cos\theta, \tag{38a}$$

$$\psi_{o_T}^{tp} = \left\{ a^2 U_{T_1}^{tp} \left[\left(\frac{a}{r}\right)^2 - 1 \right] + a^2 U_{T_2}^{tp} \Big[-3(3\widetilde{\mu}+2) \left(\frac{a}{r}\right)^2 + (19\widetilde{\mu}+16) \Big] \right\} \sin^2\theta\cos\theta, \tag{38b}$$

where

$$U_{T_1}^{tp} = U_m \sqrt{\Pi^2+1}\cos\left(2\omega t - \alpha_{T_1}\right), \quad 0 \le \alpha_{T_1} \le \pi/2, \tag{39a}$$

$$\sin\alpha_{T_1} = \frac{\Pi}{\sqrt{\Pi^2+1}}\frac{(\widetilde{\sigma}+2)(2\widetilde{\epsilon}-\widetilde{\sigma}+2) + \Pi^2(\widetilde{\epsilon}+2)^2}{\Lambda}, \tag{39b}$$

$$\cos\alpha_{T_1} = \frac{1}{\sqrt{\Pi^2+1}}\frac{(\widetilde{\sigma}+2)^2 + \Pi^2(\widetilde{\epsilon}+2)(2\widetilde{\sigma}-\widetilde{\epsilon}+2)}{\Lambda}, \tag{39c}$$

$$U_{T_2}^{tp} = -\frac{3a\omega Ca_f}{80(\widetilde{\mu}+1)}|d_T^*|\sin\left(2\omega t + \alpha_{T_2}\right), \tag{39d}$$

$$\sin\alpha_{T_2} = \frac{d_{T_I}}{|d_T^*|}, \tag{39e}$$

$$\cos\alpha_{T_2} = \frac{d_{T_R}}{|d_T^*|}, \tag{39f}$$

and the expressions for $|d_T^*|$, d_{T_I}, and d_{T_R} are given in appendix B.

Here, the velocity field comprises two components. The first component (the first bracket) is the flow driven by the net hydrodynamic shear stress $[\![\tau_{r\theta}^h]\!]_{tp}^T$, which does not lead to the drop deformation, while the second component is the flow driven by the net hydrodynamic normal stress $[\![\tau_{rr}^h]\!]_{tp}^T - [\![p]\!]_{tp}^T \equiv [\![\sigma_{rr}^h]\!]_{tp}^T$, which leads to the deformation.

The drop deformation is found from $\mathcal{D}_T^{tp} = \mathbb{R}\mathrm{e}(\mathcal{D}_T^{tp^*} e^{2i\omega t})$, where $\mathcal{D}_T^{tp^*} = (9/32)Ca_f d_T^*$. This yields

$$\mathcal{D}_T^{tp} = \frac{9}{32} Ca_f \Phi_T^{tp}, \tag{40a}$$

$$\Phi_T^{tp} = |d_T^*| \cos\left(2\omega t + \alpha_{T_2}\right), \tag{40b}$$

where Φ_T^{tp} is the characteristic function that determines the instantaneous sense of the drop deformation due to the time-periodic net electric shear stress $[\![\tau_{r\theta}^e]\!]_{tp}$. It is to be noted that

$$|U_{T_2}^{tp}| \sim \left| \frac{\partial \mathcal{D}_T^{tp}}{\partial t} \right|.$$

Thus, when the rate of the deformation is zero (at the minimum and maximum points of the $\mathcal{D}_T^{tp}$-t curve), the second bracket in eq. (38) is zero.

4.3 Fluid flow and drop deformation due to the time-periodic net normal electric stress, $[\![\tau_{rr}^e]\!]_{tp}$

We refer to the drop deformation and the velocity field due to $[\![\tau_{rr}^e]\!]_{tp}$ as the normal stress-driven deformation and flow, respectively. The detail of the solution is given in appendix C. Here the streamfunction is

$$\psi_{i_N}^{tp} = a^2 U_N^{tp} \left[(16\widetilde{\mu} + 19) \left(\frac{r}{a}\right)^3 - 3(2\widetilde{\mu} + 3) \left(\frac{r}{a}\right)^5 \right] \times \sin^2\theta \cos\theta, \tag{41a}$$

$$\psi_{o_N}^{tp} = a^2 U_N^{tp} \left[-3(3\widetilde{\mu} + 2) \left(\frac{a}{r}\right)^2 + (19\widetilde{\mu} + 16) \right] \times \sin^2\theta \cos\theta, \tag{41b}$$

$$U_N^{tp} = -\frac{3a\omega Ca_f}{80(\widetilde{\mu} + 1)} |d_N^*| \sin\left(2\omega t + \alpha_N\right), \tag{41c}$$

$$\sin\alpha_N = \frac{d_{N_I}}{|d_N^*|}, \tag{41d}$$

$$\cos\alpha_N = \frac{d_{N_R}}{|d_N^*|}, \tag{41e}$$

and the expressions for $|d_N^*|$, d_{N_I}, and d_{N_R} are given in appendix C.

The drop deformation is found using $\mathcal{D}_N^{tp} = \mathbb{R}\mathrm{e}(\mathcal{D}_N^{tp^*} e^{2i\omega t})$, where $\mathcal{D}_N^{tp^*} = (9/32)Ca_f d_N^*$. This yields

$$\mathcal{D}_N^{tp} = \frac{9}{32} Ca_f \Phi_N^{tp}, \tag{42a}$$

$$\Phi_N^{tp} = |d_N^*| \cos\left(2\omega t + \alpha_N\right), \tag{42b}$$

where Φ_N^{tp} is the characteristic function, which determines the instantaneous sense of the drop deformation due to the time-periodic net normal electric stress $[\![\tau_{rr}^e]\!]_{tp}$. It is to be noted that

$$|U_N^{tp}| \sim \left| \frac{\partial \mathcal{D}_N^{tp}}{\partial t} \right|.$$

Thus, when the rate of the deformation is zero, $\psi_N^{tp} = 0$.

5 The deformation-circulation map

The mean (time-independent) deformation $\mathcal{D}_m$ is characterized by the EHD capillary number Ca_f and the deformation characteristic function Φ_m. The parameters that control the latter are $\widetilde{\sigma} = \sigma_i/\sigma_o$, $\widetilde{\epsilon} = \epsilon_i/\epsilon_o$, and $\Pi = \epsilon_o\omega/\sigma_o$. The sign of Φ_m determines the sense of the mean deformation. For $\Phi_m > 0$ the drop becomes prolate, for $\Phi_m < 0$ it becomes oblate, and for $\Phi_m = 0$ it remains spherical. When $\Phi_m = 0$, the mean drop shape is spherical regardless of the field. In that case, the drop will oscillate about a spherical shape. Setting $\Phi_m = 0$ in eq. (35b) leads to a critical frequency

$$\omega_{cr} = \frac{\sigma_o}{\epsilon_o} \frac{\sqrt{\widetilde{\epsilon}(19\widetilde{\mu}+16) - 5(\widetilde{\mu}+1) - 3\widetilde{\sigma}(3\widetilde{\mu}+2) - 5\widetilde{\sigma}^2(\widetilde{\mu}+1)}}{|\widetilde{\epsilon} - 1|\widetilde{\sigma}\sqrt{5(\widetilde{\mu}+1)}} \tag{43}$$

at which the drop remains spherical. The existence of the critical frequency implies that the sense of mean deformation (oblate *vs.* prolate) will switch at this frequency. The critical frequency, however, exists for a certain class of fluid systems only; the one for which the expression under the square root in the numerator of eq. (43) is positive; *i.e.*,

$$\widetilde{\epsilon} \geq \widetilde{\sigma} + \frac{5(\widetilde{\mu}+1)(\widetilde{\sigma}-1)^2}{19\widetilde{\mu}+16}. \tag{44}$$

It is insightful to recast eq. (43) in the following form:

$$\omega_{cr} = \frac{\sigma_o}{\epsilon_o} \frac{\sqrt{-(\widetilde{\sigma}+2)^2 \Phi_0}}{|\widetilde{\epsilon} - 1|\widetilde{\sigma}\sqrt{5(\widetilde{\mu}+1)}}, \tag{45}$$

which suggests that in fluid systems in which the drop deforms to an oblate ($\Phi_0 < 0$) under a uniform DC electric field ($\omega = 0$), the drop may deform to an oblate ($\Phi_m < 0$) or a prolate ($\Phi_m > 0$) in a uniform AC field, depending on the field frequency ω. It can also be inferred that $\Phi_0 = 0$, results in $\Phi_m = 0$. Examination of eq. (35) shows that for $\widetilde{\sigma} > \widetilde{\epsilon}$, $\partial\Phi_m/\partial\omega < 0$, while the opposite holds for $\widetilde{\sigma} < \widetilde{\epsilon}$. Since $\mathcal{D}_m$ and Φ_m have the same sign, the same can be said regarding the sign of $\partial\mathcal{D}_m/\partial\omega$. From eq. (32) it is seen that when $\widetilde{\epsilon} = \widetilde{\sigma}$, then $U_m = 0$, and therefore, the mean flow will be null. In this context, the $\widetilde{\epsilon} = \widetilde{\sigma}$ line is called the zero-circulation line. In a $\widetilde{\epsilon} - \widetilde{\sigma}$ coordinate, the $\Phi_0 = 0$ curve and the $\widetilde{\epsilon} = \widetilde{\sigma}$ line are tangent to each other and divide the plane into three regions, each characterizing a class of fluid systems with common sense of mean deformation and mean fluid flow circulation. This is illustrated

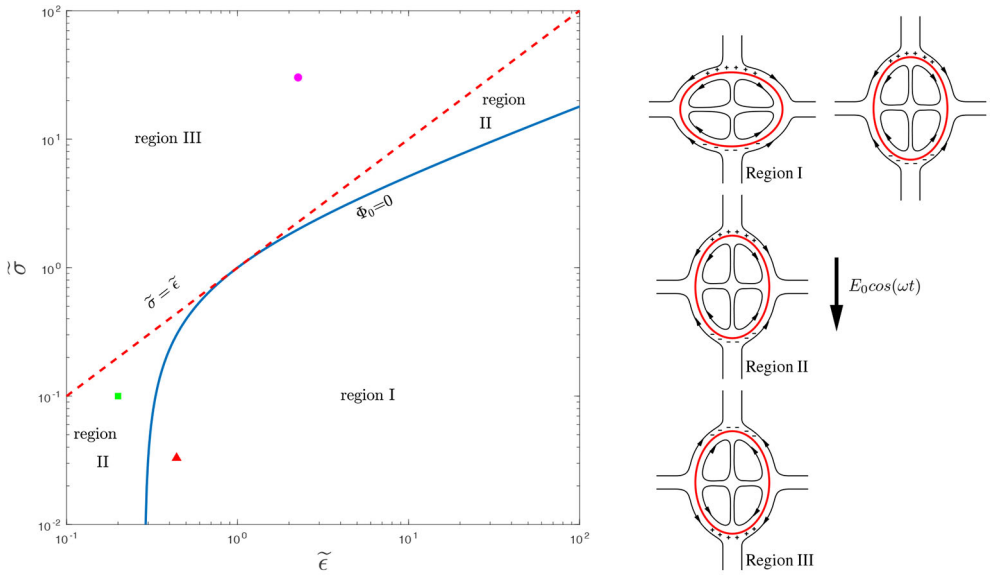

Fig. 2. The deformation-circulation map along with the schematics of the modes of mean (time-independent) deformation and mean flow pattern. The coordinates of the fluid systems *A*–*C* are, respectively, $\widetilde{\epsilon}=0.44$, $\widetilde{\sigma}=0.033$ (triangle), $\widetilde{\epsilon}=0.2$, $\widetilde{\sigma}=0.1$ (square), and $\widetilde{\epsilon}=2.2727$, $\widetilde{\sigma}=30$ (circle).

in fig. 2 and summarized below:

$$\text{region } \mathbf{I}: \quad \widetilde{\epsilon} \geq \widetilde{\sigma} + \frac{5(\widetilde{\mu}+1)(\widetilde{\sigma}-1)^2}{19\widetilde{\mu}+16}, \quad \partial \mathcal{D}_m/\partial\omega > 0, \quad \begin{cases} \mathcal{D}_m \leq 0, & \text{if } \omega \leq \omega_{cr}, \\ \mathcal{D}_m > 0, & \text{if } \omega > \omega_{cr}; \end{cases} \tag{46a}$$

$$\text{region } \mathbf{II}: \quad \widetilde{\sigma} < \widetilde{\epsilon} < \widetilde{\sigma} + \frac{5(\widetilde{\mu}+1)(\widetilde{\sigma}-1)^2}{19\widetilde{\mu}+16}, \quad \partial \mathcal{D}_m/\partial\omega > 0, \quad \mathcal{D}_m > 0; \tag{46b}$$

$$\text{region } \mathbf{III}: \quad \widetilde{\sigma} \geq \widetilde{\epsilon}, \quad \partial \mathcal{D}_m/\partial\omega \leq 0, \quad \mathcal{D}_m \geq 0. \tag{46c}$$

6 Summary of the solution

The overall streamfunction is found from substitution of the time-exponential and the time-periodic shear stress- and normal stress-driven streamfunctions, using eqs. (31), (38), and (41), in eq. (26).

The overall deformation is found from superposition of the time-exponential and the time-periodic shear stress- and normal stress-driven deformations, using eqs. (34), (40), (42), leading to

$$\mathcal{D} = \mathcal{D}_{te} + \mathcal{D}^{tp} = \frac{9}{32} Ca_f \Phi, \tag{47a}$$

$$\mathcal{D}^{tp} = \mathcal{D}_T^{tp} + \mathcal{D}_N^{tp} = \frac{9}{32} Ca_f \Phi_{tp}, \tag{47b}$$

$$\Phi = \Phi_m[1-\exp(-t/\tau)] + \Phi_{tp}, \tag{47c}$$

where

$$\Phi_{tp} = \Phi_T^{tp} + \Phi_N^{tp} = |d^*| \cos(2\omega t + \alpha_{TN}), \tag{48a}$$

$$d^* = d_R + i d_I, \qquad |d^*| = \sqrt{d_R^2 + d_I^2}, \tag{48b}$$

$$\cos\alpha_{TN} = \frac{d_R}{|d^*|}, \qquad \sin\alpha_{TN} = \frac{d_I}{|d^*|}, \tag{48c}$$

$$d_R = \frac{d_{N_{R_1}} + d_{N_{R_2}} + d_{N_{R_3}} - d_{N_{R_4}} + d_{T_{R_1}} - d_{T_{R_2}}}{\Lambda^2(1+Ca_\omega^2\lambda_2^2)}, \tag{48d}$$

$$d_I = -\frac{d_{N_{I_1}} + d_{N_{I_2}} + d_{N_{I_3}} + d_{N_{I_4}} + d_{T_{I_1}} + d_{T_{I_2}}}{\Lambda^2(1+Ca_\omega^2\lambda_2^2)}, \tag{48e}$$

and the expressions for the terms comprising d_R and d_I are given in appendices B and C.

7 Torza et al. [8] solution

Torza *et al.* did not account for the transient period. As such, their solution is valid for times that are sufficiently larger than the deformation relaxation time. Their decomposition of the solution based on the drivers of the problem was exactly the same as that outlined here. Their solution for the mean component is the same as ours (the first bracket of eq. (31)), as their jump conditions were the same as those used in appendix A in the limit of $t \to \infty$. However, their solutions for the other components differ from ours. Briefly, for the solution due to $[\![\tau_{r\theta}^e]\!]_{tp}$, they used jump conditions I and III in appendix B, while they used $u_{r_i}^T = u_{r_o}^T = 0$ in lieu of jump condition II. Thus, they did not need to find the time-periodic deformation $\mathcal{D}_T^{tp}$ and could determine the velocity field without using jump condition IV. Their solution led to the first bracket in eq. (38). For the solution due to $[\![\tau_{rr}^e]\!]_{tp}$, they used jump conditions I-III in appendix C, but in lieu of jump condition IV, they used the following jump condition:

$$[\![\tau_{rr}^e]\!]_{tp} + [\![\tau_{rr}^h]\!]_{tp}^N - [\![p]\!]_{tp}^N + [\![\tau_{rr}^h]\!]_{tp}^T - [\![p]\!]_{tp}^T = \gamma\kappa^{tp}.$$

This equation accounts for the contribution of the net normal hydrodynamic stresses (the fourth and fifth terms) due to the net electric shear stress $[\![\tau^e_{r\theta}]\!]_{tp}$ in the deformation. This led to an equation for the streamfunction that was formally the same as ours (eq. (41)), except that $|d^*_N|$ in their version of eq. (41) was replaced with $|d^*|$ from eq. (48). The time-periodic deformation $\mathcal{D}^{tp}_N$ was also found as part of this solution. In summary, their streamfunction and deformation, respectively, can be perceived as

$$\psi = \underbrace{\psi_m}_{\text{First bracket of eq. (31)}} + \underbrace{\psi^{tp}_T}_{\text{First bracket of eq. (38)}} + \underbrace{\psi^{tp}_N}_{\text{Second bracket of eq. (38) plus eq. (41)}}, \tag{49a}$$

$$\mathcal{D} = \underbrace{\mathcal{D}_m}_{\text{eq. (35a)}} + \underbrace{\mathcal{D}^{tp}_T}_{0} + \underbrace{\mathcal{D}^{tp}_N}_{\text{eq. (47b)}}. \tag{49b}$$

The distribution of the electric potential at the drop surface is of interest as it provides insight on the interfacial electric stresses, which are the driver behind the fluid flow circulation and interface deformation. As is evident from eqs. (14)–(17), the ratios of electric conductivities $\widetilde{\sigma} = \sigma_i/\sigma_o$ and permittivities $\widetilde{\epsilon} = \epsilon_i/\epsilon_o$, and the nondimensional frequency $\mathit{\Pi} = \epsilon_o\omega/\sigma_o$ are the key parameters that affect the structure of ϕ (**E**) in the fluids and at the interface. For $\omega = 0$ and $\omega \to \infty$, ϕ (**E**) will be only function of $\widetilde{\sigma}$ and $\widetilde{\epsilon}$, respectively [25]. Here we examine the evolution of ϕ and **E** for fluid systems A and C (table 1), where fluid system C is the phase-reversed of fluid system A. These two systems represent fluid systems for which ($\widetilde{\sigma} \ll 1$, $\widetilde{\epsilon} \lessapprox O(1)$) and ($\widetilde{\sigma} \gg 1$, $\widetilde{\epsilon} \gtrapprox O(1)$), respectively. We consider $\omega = 2\,\text{rad/s}$, resulting in $\mathit{\Pi} = 0.116$ for fluid system A, and $\mathit{\Pi} = 0.116$ for fluid system C. To put the results in perspective, the distribution of ϕ and **E** for a DC electric field are shown in fig. 3. For system A, the external contours in the proximity of the drop bend as they approach the drop surface before crossing the surface. The contours inside the drop are horizontal and their concentration is higher than that in the rest of the domain, since $\sigma_i \ll \sigma_o$. For the same reason, the electric field vectors near the drop do not cross the drop; instead, they turn around it. For system C, the electric potential inside the drop vanishes and the drop surface becomes a surface of equipotential. As such, the contourlines near the drop conform to its shape. Because the net electric stresses are determined by the field strength across the interface, per eq. (19), a drop in fluid system A is subjected to a relatively weak electric stress and therefore is deformed less than the one in fluid system C. Since the net tangential electric stress, which set the fluid into motion, is determined by the product of the tangential electric field and free surface charge, significant EHD-driven flows are expected to occur in fluid system A in which the more conductive fluid is the continuous phase, compared to fluid system C.

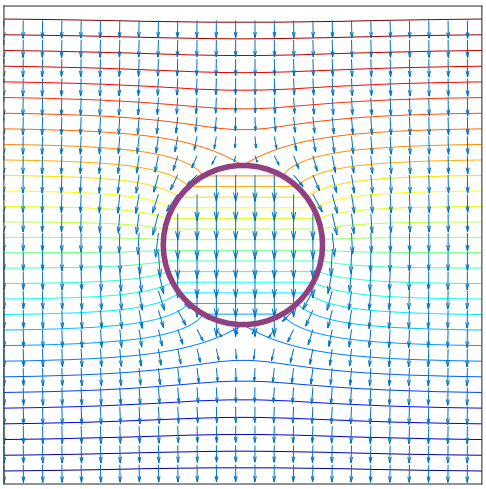

(a)

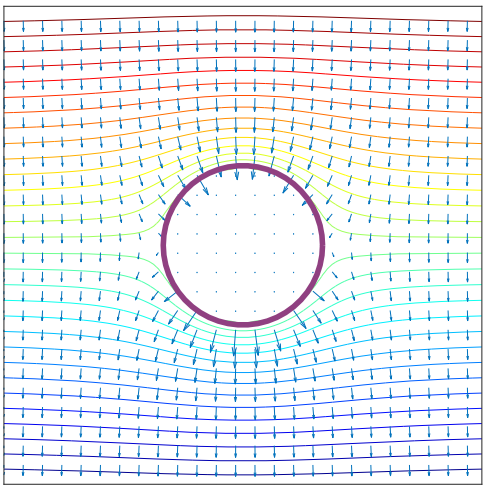

(b)

Fig. 3. Contours of electric potential ϕ and vectors of electric field strength **E** for fluid systems A (frame (a)) and C (frame (b)) in a DC ($\omega = 0$) electric field. The fluid properties are listed in table 1. Note that fluid system C is the phase-reversed of fluid system A.

Table 1. Relevant information about the representative fluid systems used to study the evolution of the electric field and the velocity field in the three regions of the deformation-circulation map. System A corresponds to silicon oil (inside) surrounded by oxidized castor oil (outside), and system C is the phase-reversed of system A. The properties for systems A and C are adopted from Torza *et al.* [8], while system B is conceptual.

Fluid system	Region	$\widetilde{\sigma}$	$\widetilde{\epsilon}$	$\widetilde{\rho}$	$\widetilde{\mu}$
A	**I**	0.033	0.44	1	1.8462
B	**II**	0.1	0.2	1	1
C	**III**	30	2.2727	1	0.5417

8 Results

Figure 4 shows the results for the fluid system A at selected nondimensional ($\widetilde{t} = \omega t$) times. The structure of ϕ

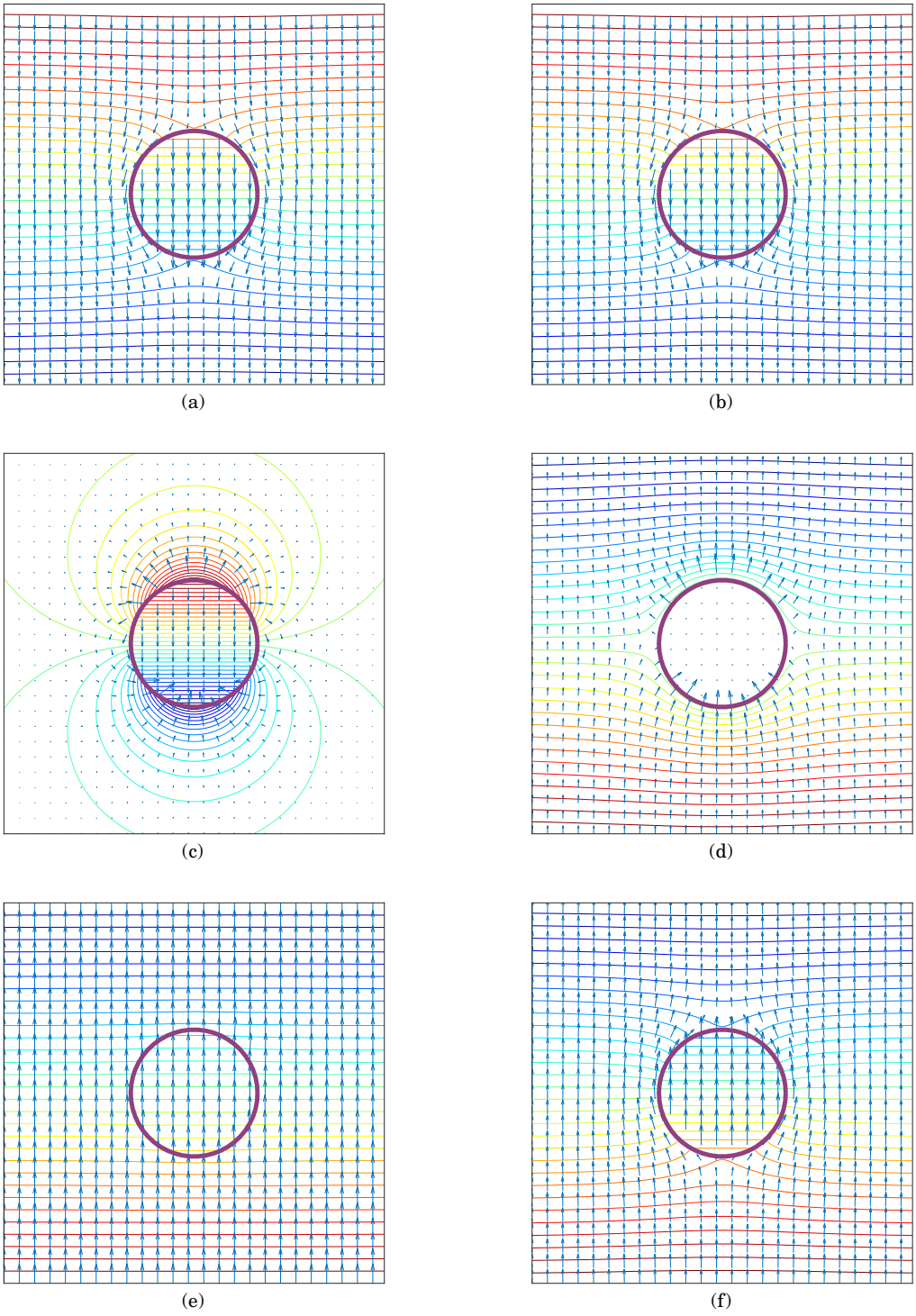

Fig. 4. Contours of electric potential ϕ and vectors of electric field strength $\mathbf{E}$ for fluid systems A (table 1) during a half cycle, $\omega t = \pi$. The nondimensional times $\widetilde{t} = \omega t$ are 0, $\alpha_{E_i} = 0.022$, $\pi/2$, $\pi/2 + \alpha_{E_i}$, 0.52π, and π, where α_{E_i} is the phase lag of $\mathbf{E}_i$ with respect to $\mathbf{E}_{ext}$, per eq. (16).

and $\mathbf{E}$ for frame (a), $\widetilde{t} = 0$, is quite similar to the corresponding ones for the DC electric field (fig. 3(a)). This is because for the range of the parameters used here, A^* in eq. (15), which determines the structure of ϕ in AC field, is approximately the same as $1/(\widetilde{\sigma} + 2)$, which determines the structure of ϕ in a DC field. Frame (b) corresponds to $\widetilde{t} = \alpha_{E_i}$, where the strength of the internal electric field $|\mathbf{E}_i|$ is maximum, per eq. (16). Here $\alpha_{E_i} = 0.022$ rad and the results are essentially the same as those for frame (a), since the phase lag is very small. We note that if vector plot of the electric current density $\mathbf{J} = \sigma\mathbf{E}$ is used instead of $\mathbf{E}$, the contrast between the vectors in the drop for the two frames will be more pronounced. Frame (c) corresponds to $\widetilde{t} = \pi/2$ where the imposed electric field

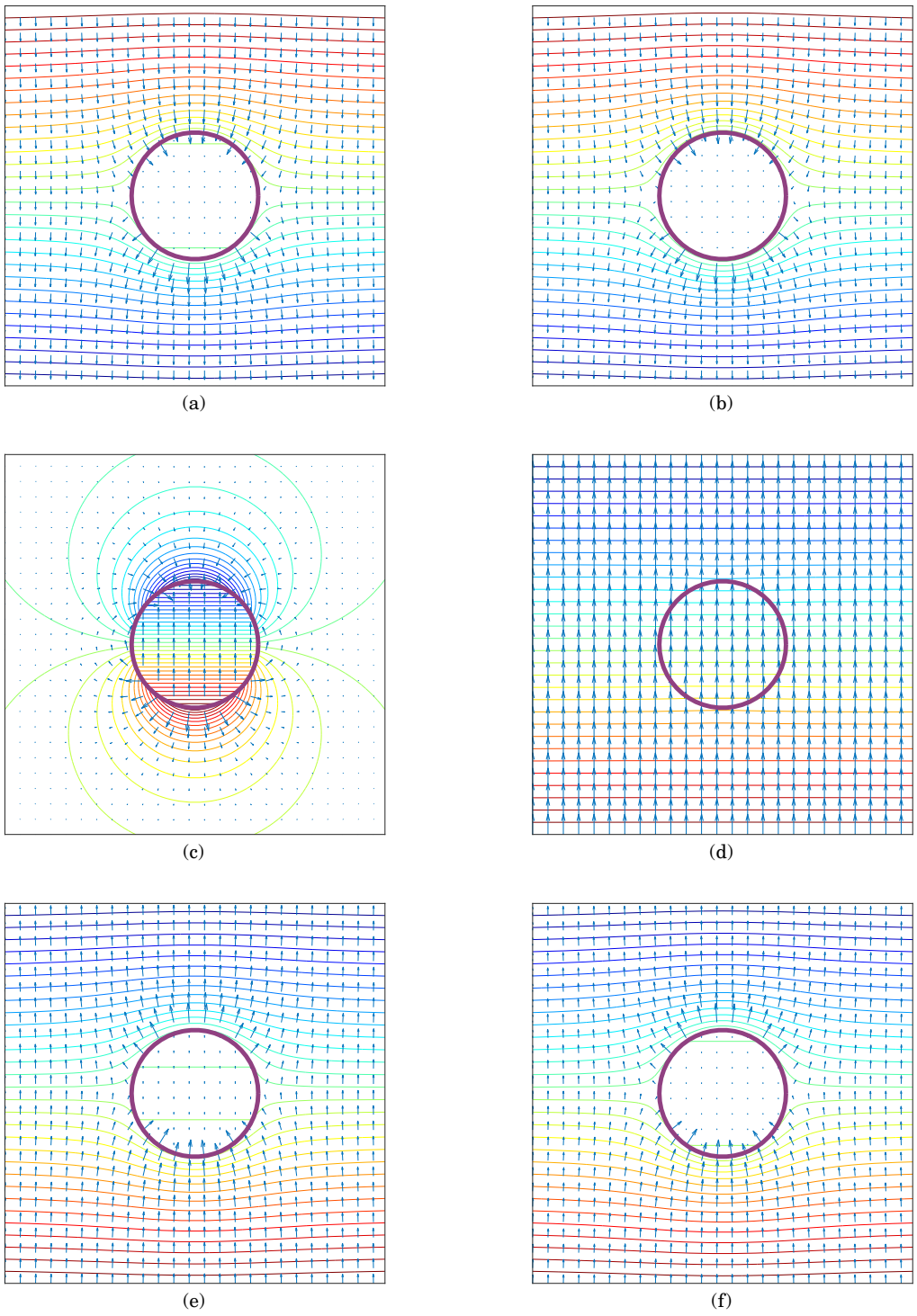

Fig. 5. Contours of electric potential ϕ and vectors of electric field strength $\mathbf{E}$ for fluid systems C (table 1) during a half cycle, $\omega t = \pi$. The nondimensional times $\widetilde{t} = \omega t$ are 0, $\pi/2 + \alpha_{E_i}$, $\pi/2$, 0.54π, $\pi + \alpha_{E_i}$, and π, where $\alpha_{E_i} = -0.78$ is the phase difference between $\mathbf{E}_i$ and $\mathbf{E}_{ext}$, per eq. (16).

strength is zero, $|\mathbf{E}_{ext}| = 0$. Here while ϕ and $\mathbf{E}$ are weak, they are not zero because of their phase lag with respect to $\mathbf{E}_{ext}$. The direction of electric potential gradient in the drop is the opposite of those in the ambient fluid right above and below the drop, in contrast to the previous frames. As a result, the vectors of electric field emanate from the northern hemisphere and cross into the southern hemisphere along circular paths. However, they do not lead to "closed" counter-rotating vortices. Frame (d) corresponds to $\widetilde{t} = \alpha_{E_i} + \pi/2$ where the strength of the internal electric field is zero, $|\mathbf{E}_i| = 0$, per eq. (16). Here since the electric field vanishes in the drop, the drop surface becomes a surface of equipotential. Thus, the electric potential contours go around the surface of the drop.

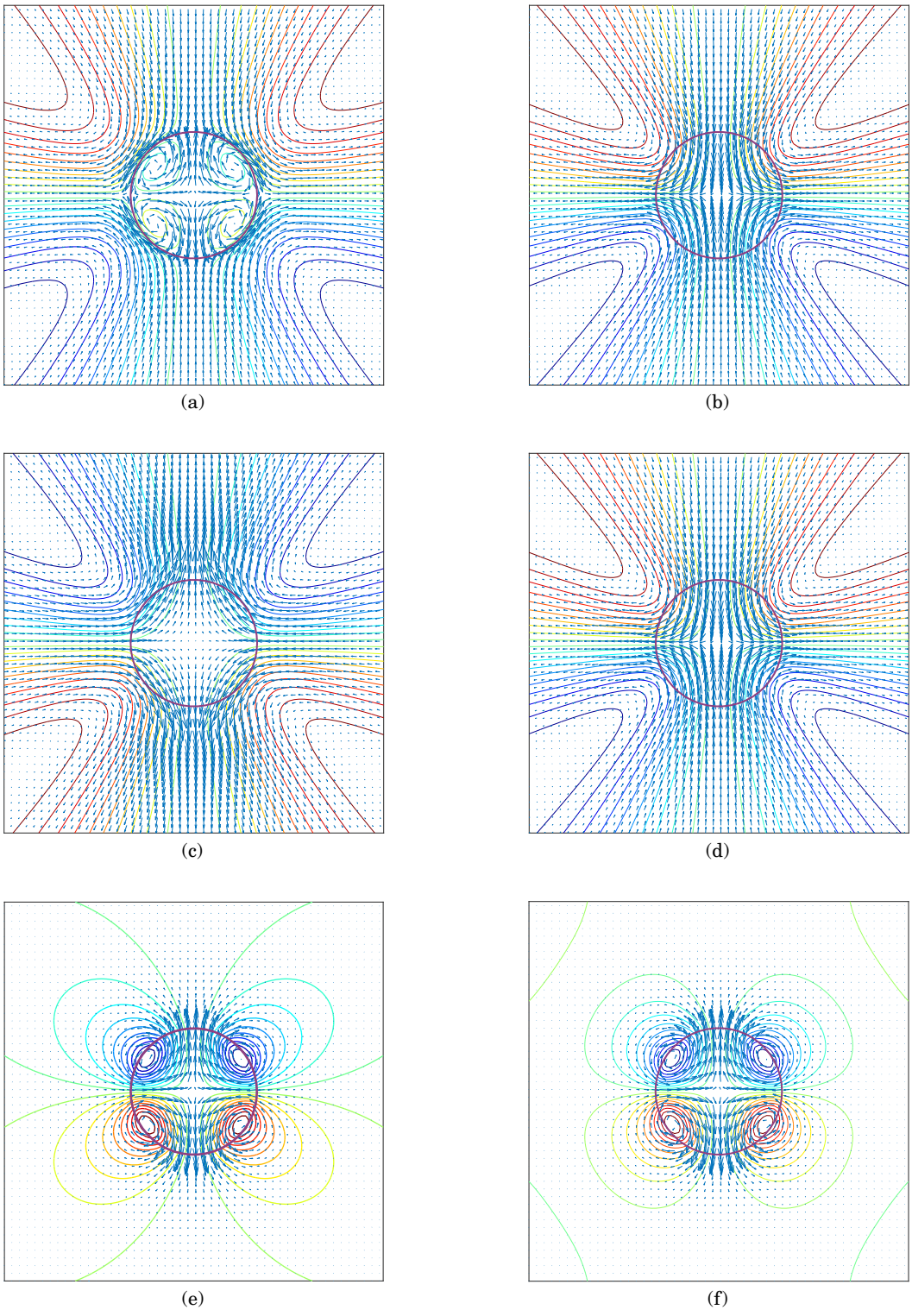

Fig. 6. Velocity streamlines at $\widetilde{t} = 1.0714$ for fluid system A under a field of frequency $\omega = 1\,\mathrm{rad/s}$ ($\Pi = 0.0558$), using the present solution. Frames (a) and (b) show the mean and the time-exponentially decaying flows, corresponding to the first and the second brackets in eq. (31), respectively. Frames (c) and (d) show the shear stress- and normal stress-driven flows, corresponding to eqs. (38) and (41), respectively. Frame (e) shows the overall flow pattern, excluding the time-exponentially decaying part, resulting from superposition of frames (a), (c), and (d), and frame (f) shows the overall flow pattern, resulting from superposition of frames (a)–(d).

Frame (e) corresponds to $\widetilde{t} \approx 0.52\pi$, which is slightly after the time of frame (d), and for which the strength of the induced electric dipole is weak, per eq. (17). Here the contour lines are nearly horizontal and the structures of ϕ and $\mathbf{E}$ resemble the corresponding ones for a uniform electric field in the absence of the drop. Frame (f) corresponds to $\widetilde{t} = \pi = T/2$, T being the period of the imposed electric field $\mathbf{E}_{ext}$. Here the results are similar to those for frames (a) and (b), except for the fact that the polarities of the electrodes are now the opposite.

Figure 5 shows the results for the phase-reversed case. The structures of ϕ and $\mathbf{E}$ for frame (a), $\widetilde{t} = 0$, are similar to the corresponding ones in fig. 3(b). As before, this is because here A^* in eq. (15), which determines the structure of ϕ in AC field, is approximately the same as $1/(\widetilde{\sigma} + 2)$, which determines the structure of ϕ in a DC field. Frame (b) corresponds to $\widetilde{t} = \pi/2 + \alpha_{E_i}$, where $|\mathbf{E}_i| = 0$, per eq. (16). Here $\alpha_{E_i} = -0.78\,\text{rad}$ and the structures of ϕ_o and $\mathbf{E}_o$ are essentially the same as the corresponding ones for frame (a). Frame (c) corresponds to $\widetilde{t} = \pi/2$, where $|\mathbf{E}_{ext}| = 0$. Again, because of the phase difference between ϕ ($\mathbf{E}$) and $\mathbf{E}_{ext}$, the induced electric field is weak, but not zero. Frame (d) is at $\widetilde{t} \approx 0.54\pi$, which is a time slightly greater than that of the frame (c), and for which the strength of the induced electric dipole is weak compared to that of the external electric field, per eq. (17). Here the structures of ϕ and $\mathbf{E}$ resemble those in the absence of the drop. Frame (e) corresponds to $\widetilde{t} = \pi + \alpha_{E_i}$, where $|\mathbf{E}_i|$ is maximum. Here the vectors in the drop are slightly larger than those in the previous frames, while the external field is similar to those of the first and the second frames. Frame (f) corresponds to $\widetilde{t} = \pi = T/2$, T being the period of the imposed electric field $\mathbf{E}_{ext}$. Here the results are similar to those for frames (a) and (b), except for the fact that the polarities of the electrodes are now the opposite.

We also explored the effect of ω on the structure of ϕ and $\mathbf{E}$ by considering frequencies in the range of 100–1000 rad/s, corresponding to $\mathit{\Pi} = 5.578$–55.78 (system A) and 73.63–736.3 (system C). For both fluid systems, the structures of ϕ were similar to their corresponding structures for $\omega = 2$, with the only difference being that the external contourlines were less bent. This is typical of fluid systems where conductivity and permittivity ratio are both less than or greater than one (which is the case for fluid systems A and C), since the electric field structure at both end of the spectra ($\omega = 0$ and $\omega \to \infty$) will be similar. On the other hand, the effect of frequency ω will be more pronounced for fluid systems for which ($\widetilde{\sigma} \gg 1$, $\widetilde{\epsilon} \ll 1$) or ($\widetilde{\sigma} \ll 1$, $\widetilde{\epsilon} \gg 1$).

8.1 Fluid flow structure and its evolution

EHD-driven flows in and around a liquid drop find relevance in a host of microfluidic applications, such as enhancement of fluid mixing and heat transfer by convection [16–18]. As such, a fundamental understanding of the flow field and its evolution as a function of the key controlling parameters will be helpful for an optimum design of the microfluidic devices and their operation. To this end, we have followed the evolution of the flow field for the fluid systems listed in table 1 for two different frequencies. Before attending to those results, however, it will be insightful to examine the structure of the components of the flow field at a fixed time, using eqs. (31), (38), and (41). In what follows, we refer to the flow field due to $[\![\tau^e_{r\theta}]\!]_{tp}$ (eq. (38)) as the shear stress-driven flow, and that due to $[\![\tau^e_{rr}]\!]_{tp}$ (eq. (41)) as the normal stress-driven flow.

Figure 6 shows the components of the velocity streamlines for fluid system A at $\omega = 1\,\text{rad/s}$ and $\widetilde{t} = 1.0714$. This fluid system belongs to region **I** of the deformation-circulation map. Thus, the external flow associated with the mean component will run from the poles toward the equator. The mean drop shape will be oblate ($\mathcal{D}_m < 0$) since the applied frequency is less than the critical frequency, $\omega_{cr} = 23.19\,\text{rad/s}$; see eq. (46). Here in analyzing the results it is helpful to consider fig. 7, which shows the variations of the components of the deformation, $\mathcal{D}_{te}$, $\mathcal{D}^{tp}_T$, and $\mathcal{D}^{tp}_N$, with time, and in which we mark the time (of the analysis) in order to facilitate identification of the signs of $\partial\mathcal{D}_{te}/\partial t$, $\partial\mathcal{D}^{tp}_T/\partial t$, and $\partial\mathcal{D}^{tp}_N/\partial t$ at the same time as the time of the velocity fields in fig. 6. Frame (a) of fig. 6 shows the mean flow, which corresponds to the first bracket in eq. (31). It consists of two toroidal vortices inside the drop in the upper and the lower hemispheres, which are matched by the counterpart vortices in the ambient fluid. The cross section of these vortices with the symmetry plane appears as four counter-rotating circulation regions. No streamline crosses the interface, which is in accord with the fact that the rate of mean deformation is null, $\partial\mathcal{D}_m/\partial t = 0$. Frame (b) shows the exponentially decaying component, which corresponds to the second bracket in eq. (31). Here the streamlines cross into the drop surface at the poles and exit from the equator, in line with the sign of $\partial|\mathcal{D}_{te}|/\partial t > 0$, per fig. 7. Frame (c) shows the shear stress-driven component, which corresponds to eq. (38). Here the streamlines cross into the drop surface from the equator and exit from the poles, in line with the sign of $\partial|\mathcal{D}^{tp}_T|/\partial t < 0$, per fig. 7. Frame (d) shows the normal stress-driven component, which corresponds to eq. (41). For this frame, the sense of flow circulation is the same as that of frame (b) but the opposite of that in frame (c), since the sign of $\partial|\mathcal{D}^{tp}_N|/\partial t$ is the same as the sign of $\partial|\mathcal{D}_{te}|/\partial t$ but the opposite of the sign of $\partial|\mathcal{D}^{tp}_T|/\partial t$. Frame (e) is the result of superposition of frames (a), (c), and (d), and frame (f) shows the total velocity field, resulting from the superposition of frames (a)–(d). The overall flow comprises closed vortices that cross into the surface, as opposed to open-ended streamlines. Judging by the sense of circulation of the closed vortices in the overall velocity field (frame (f)), it can be inferred that the drop is rebounding at this instant (becoming less oblate), since the sense of flow circulation favors elongation of the drop in the direction of the imposed electric field. At this instant, the mean flow (frame (a)), the time-exponentially decaying flow (frame (b)), and the normal stress-driven flow (frame (d)) tend to increase the deformation, while

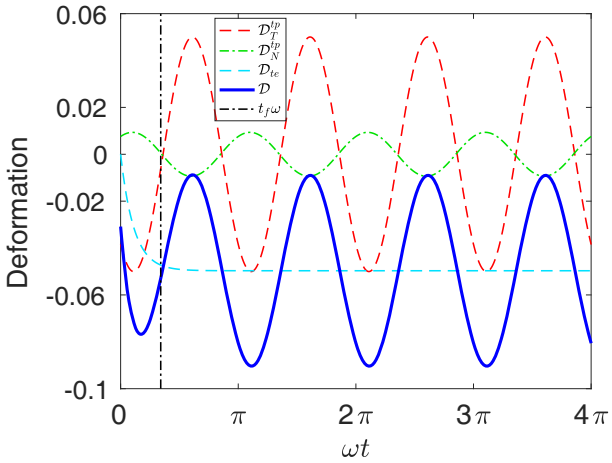

Fig. 7. Evolution of the components of the deformation *versus* nondimensional time ωt for fluid system A and electric field frequency of $\omega = 1\,\mathrm{rad/s}$. The vertical line marks the time that the velocity field is analyzed in figs. 6 and 8.

the shear stress-driven flow (frame (c)) tends to decrease it. It should be noted that except for the mean and the transient flows, the sense of circulation of the other components will change with time. In summary, the mean flow (first bracket of eq. (31)) is characterized by closed vortices inside the drop, and open-ended streamlines in the ambient that do not cross the drop, while the time-exponentially decaying (second bracket of eq. (31)) and the normal stress-driven flows (eq. (41)) are characterized by open-ended streamlines that cross the drop. On the other hand, the shear stress-driven flow (eq. (38)) can be characterized by both the closed vortices (first bracket) and the open-ended streamlines (second bracket). The overall flow field will comprise of open-ended streamlines, closed vortices, or a combination of the two, depending on the interplay of the components of the velocity field. As will be shown shortly, the interplay of the four velocity patterns over the time leads to formation and growth of closed vortices in the drop and the ambient, or their decay and destruction.

Figure 8 shows the components of the velocity field based on Torza *et al.* solution (eq. (49)). Here we do not present their mean flow ψ_m, since it is the same as ours. Frame (a) shows the shear stress-driven component ψ_T^{tp}. This flow pattern should be contrasted with that of fig. 6(c), in which the flow consisted of open-ended streamlines only. The reason that here the streamlines do not cross the drop surface is because the rate of deformation is (implicitly) assumed to be zero in their solution as discussed in sect. 7. Thus, their shear stress-driven flow pattern is always similar to that of the mean flow. However, the sense of flow circulation for this component will not be necessarily the same as that of the mean flow (at a given time) because of its time-periodic nature. Frame (b) shows the normal stress-driven component ψ_N^{tp}. This flow pattern should be contrasted with that in fig. 6(d); while the two flow patterns are quite similar, their senses of circulation at this time are the opposite. Finally, frame (c) shows the

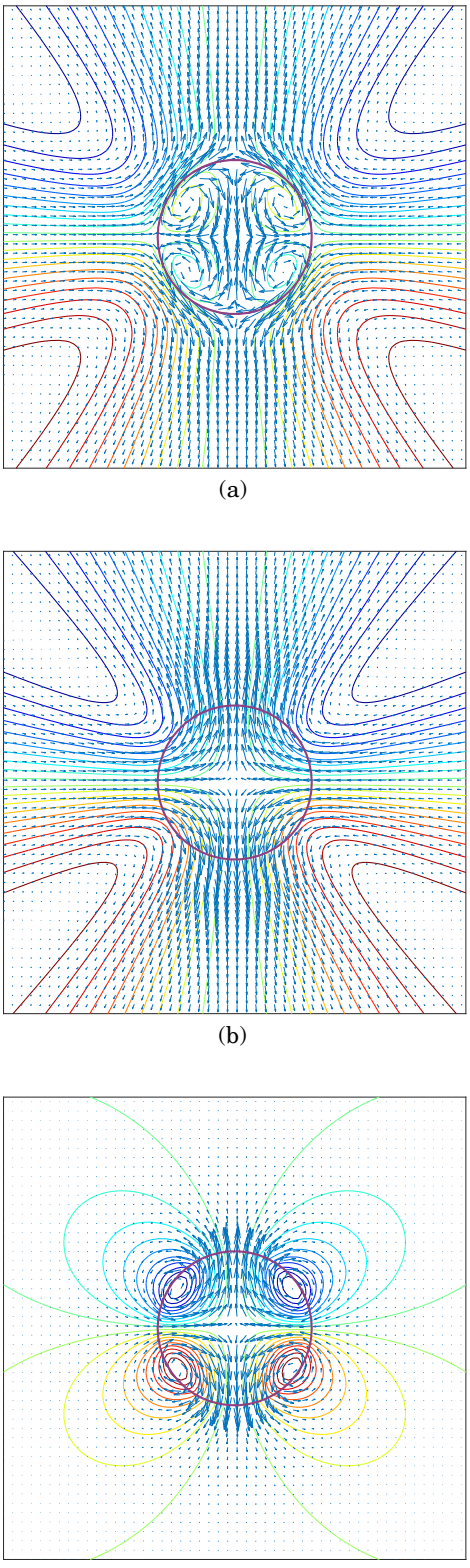

(a)

(b)

(c)

Fig. 8. Velocity streamlines at $\widetilde{t} = 1.0714$ for fluid system A under a field of frequency $\omega = 1\,\mathrm{rad/s}$, using Torza *et al.* solution. Frames (a) and (b) show the shear stress- and normal stress-driven flows, corresponding to ψ_T^{tp} and ψ_N^{tp} of eq. (49a), respectively. Frame (c) shows the overall flow pattern, corresponding to ψ of the same equation.

total velocity field, which is the result of the superposition of the mean flow (fig. 6(a)) and these two components. As expected, the overall flow pattern and its sense of circulation are exactly the same as those of ours (fig. 6(e)) at quasi–steady-state ($t \to \infty$).

In passing, we make two comments about fig. 7. First, as is evident the net electric shear and normal stresses, $[\![\tau^e_{r\theta}]\!]_{tp}$ and $[\![\tau^e_{rr}]\!]_{tp}$, can lead to opposite (instantaneous) rate of deformations. Second, the order of magnitude of the deformation due to these stresses, $\mathcal{D}^{tp}_T$ and $\mathcal{D}^{tp}_N$, are comparable. Thus, while the common perception might be that the drop deformation is primarily due to net normal electric stresses (*i.e.*, $\mathcal{D}^{tp}_N \gg \mathcal{D}^{tp}_T$), this is not true in general.

To explore the possibility of the formation of closed vortices in the drop or the ambient, we examine the possibility of formation of a dividing streamline (*i.e.*, a $\psi = 0$ closed curve), since the closed vortices are always accompanied with and confined within a dividing streamline. For the problem at hand, where the deformation is weak, the dividing streamline (in the plane of symmetry) will be always a circle. To find the radius of this circle we set $f_{i,o}(r) = 0$ in the expression for $\psi_{i,o} = f_{i,o} \sin^2\theta \cos\theta$ in eq. (26), where $f_{i,o}$ is the sum of the r-dependent terms in this equation. This yields

$$\frac{r_i}{a} = \left[\frac{U_m + U^{tp}_{T_1} + (16\widetilde{\mu}+19)(U_{te} + U^{tp}_{T_2} + U^{tp}_N)}{U_m + U^{tp}_{T_1} + 3(2\widetilde{\mu}+3)(U_{te} + U^{tp}_{T_2} + U^{tp}_N)}\right]^{1/2} \tag{50}$$

and

$$\frac{r_o}{a} = \left[\frac{U_m + U^{tp}_{T_1} - 3(3\widetilde{\mu}+2)(U_{te} + U^{tp}_{T_2} + U^{tp}_N)}{U_m + U^{tp}_{T_1} - (19\widetilde{\mu}+16)(U_{te} + U^{tp}_{T_2} + U^{tp}_N)}\right]^{1/2}, \tag{51}$$

as the radius of the dividing streamline in the drop and the ambient, respectively, provided $0 < r_i/a < 1$ and $1 < r_o/a$. For this unbounded flow, there will be at most one dividing streamline at a given time. In other words, it is not possible to have an internal and an external dividing streamline at the same time.

In what follows, we will perform frame by frame analysis of the flow fields for representative cases. To do so, we will examine concurrently the evolution of the deformation $\mathcal{D}$ and the (nondimensional) radius of the dividing streamline (r/a) with time, since these two curves provide the needed information that might not be possible to discern from the velocity snapshots. The times of the velocity snapshots are selected at the outset using the corresponding deformation-time curve, considering a cycle during which the drop deformation changes from the minimum (starting point) to the maximum (ending point), in an absolute sense. Furthermore, the cycle is selected in the quasi-steady region, so that the transient effects are essentially diminished. On the basis of the sign of $\partial|\mathcal{D}|/\partial t$ being positive or negative, two stages or half-cycles can be recognized in the $\mathcal{D}$-t curve; a deformation stage, where the deformation of the drop increases (in an absolute sense) from the minimum to the maximum, and a rebound stage, where the reverse process happens.

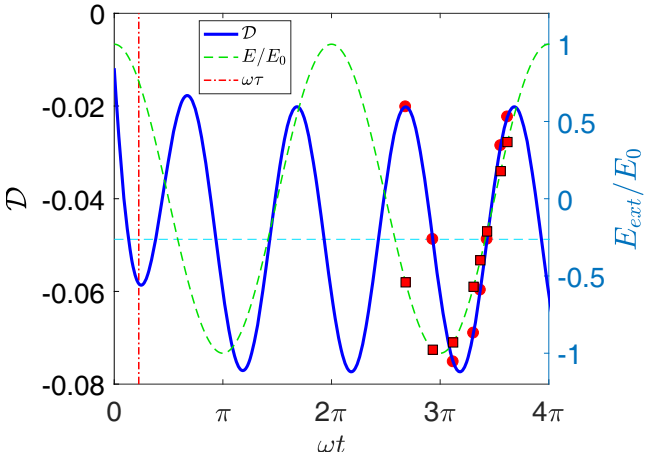

Fig. 9. Evolution of the total deformation $\mathcal{D}$ *versus* nondimensional time ωt for fluid system A and electric field frequency of $\omega = 2\,\mathrm{rad/s}$. The markers identify $\mathcal{D}$ and E_{ext} at times that correspond to the velocity snapshots in fig. 10. The horizontal line represents the mean deformation $\mathcal{D}_m$ and the dash-dotted vertical line marks the nondimensional deformation relaxation time $\omega\tau$, where τ is given by eq. (35c).

8.1.1 Region I (fluid system A)

We start our analysis by considering the evolution of the flow field for fluid system A, under an electric field of low frequency ($\omega = 2\,\mathrm{rad/s}$), corresponding to $\Pi = 0.1116$. Figures 9–11 show the pertinent results. This is the same fluid system that we just used to examine the structure of the components of the flow field. Thus, the mean drop shape will be oblate and the mean external fluid will run from the poles toward the equator, in line with the inset of fig. 2. Since the mean drop shape is oblate ($\mathcal{D}_m = -0.0488 < 0$), the maxima and the minima on the $\mathcal{D}$-t curve correspond, respectively, to the minimum and maximum deformations in an absolute sense. Here the drop remains oblate at all times (fig. 9), however, if the time-periodic deformation $\mathcal{D}_{tp} = \mathcal{D}^T_{tp} + \mathcal{D}^N_{tp}$ were greater than the time-exponential deformation $\mathcal{D}_{te}$, the drop would oscillate between an oblate and a prolate shape. The drop deformation relaxes to its mean over two oscillation cycles.

Figure 10 shows the flow pattern at the selected times noted in the caption, where the dividing streamline (when it exists) is shown by a dashed line. In frame (a), the flow pattern is quite similar to that for a drop in a DC electric field, with no streamline crossing the drop surface. This is because at this time, the rate of the deformation is zero, $\partial\mathcal{D}/\partial t = 0$, since the drop deformation is minimum as is evident from fig. 9. When $\partial\mathcal{D}/\partial t = 0$, ψ^{tp}_N and the second brackets of ψ_{te} and ψ^{tp}_T will be zero. Thus, the flow pattern will be similar to that for a DC electric field; however, the sense of flow circulation will not be necessarily the same. Here the dividing streamline resides on the surface of the drop. As the deformation increases, the external streamlines gradually move toward the drop surface and eventually cross the surface (frame (b)), thus,

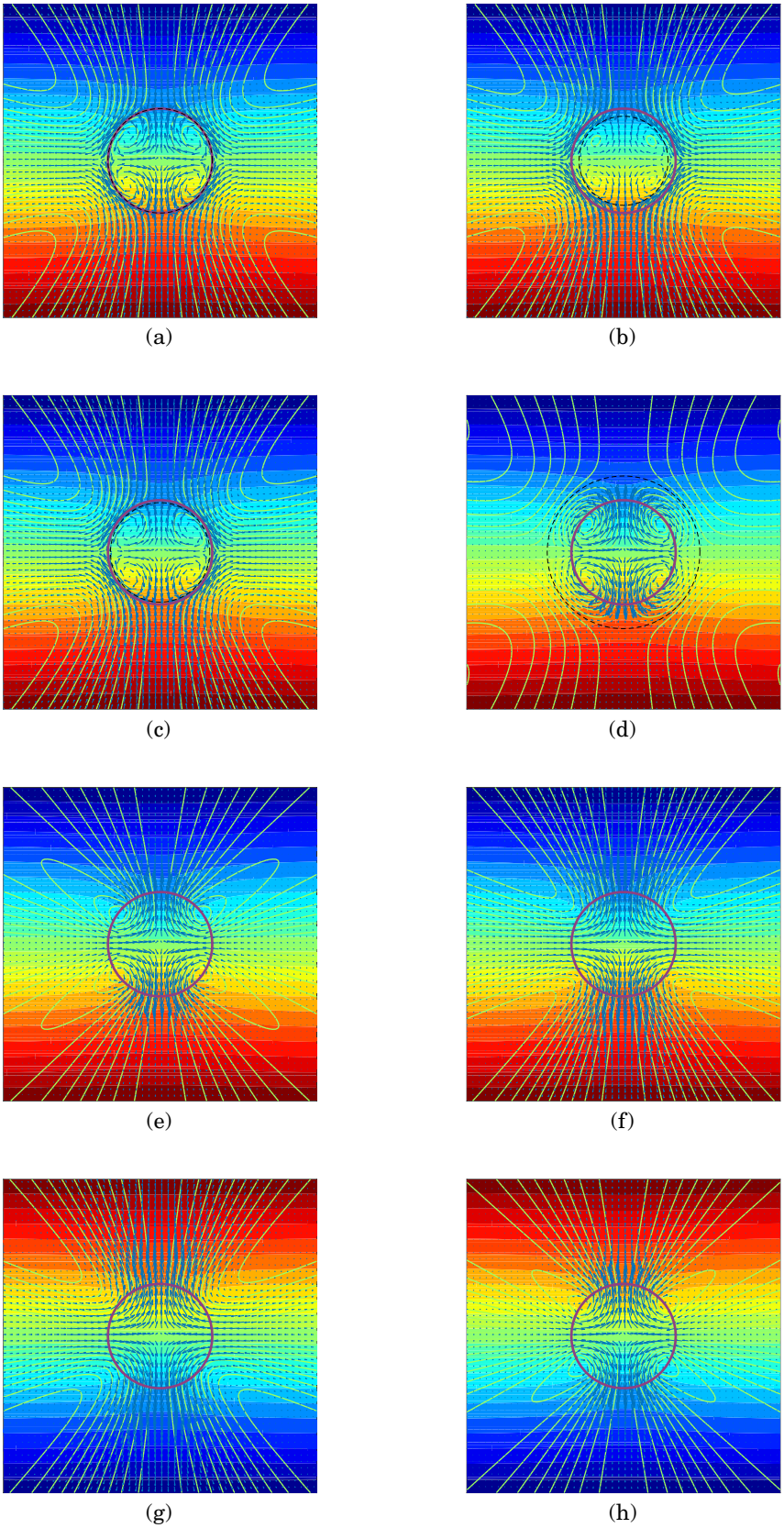

Fig. 10. Vector plot of the velocity field along with the velocity streamlines and contours of the electric potential ϕ for fluid system A and electric field frequency of $\omega = 2\,\mathrm{rad/s}$, corresponding to $\Pi = 0.1116$. The frames correspond to the markers in fig. 9.

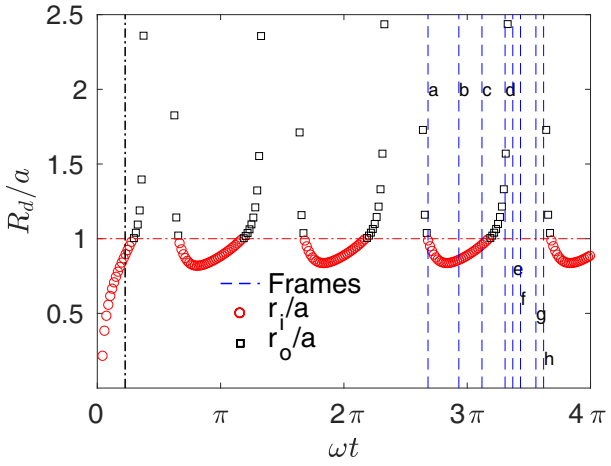

Fig. 11. Evolution of the dividing streamline, r_i/a, r_o/a, with time for fluid system A and electric field frequency of $\omega = 2\,\text{rad/s}$. The dashed vertical lines mark the times of the velocity snapshots in fig. 10. The dash-dotted vertical line marks the nondimensional deformation relaxation time $\omega\tau$, where τ is given by eq. (35c).

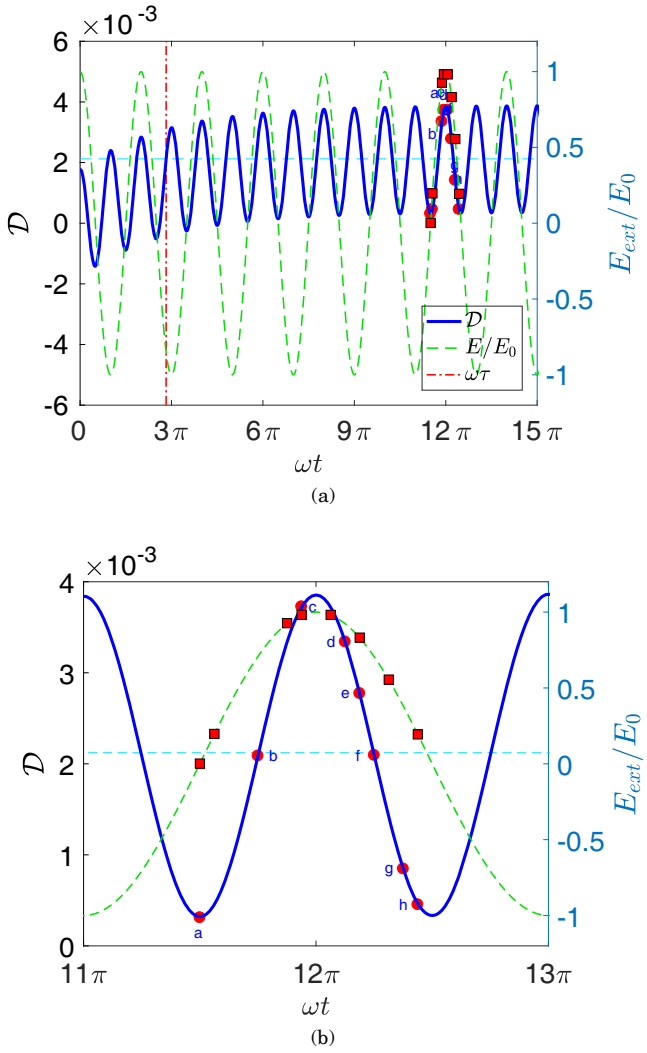

Fig. 12. Evolution of the total deformation $\mathcal{D}$ *vs.* nondimensional time ωt for fluid system A and electric field frequency of $\omega = 25\,\text{rad/s}$ (frame (a)). The markers identify $\mathcal{D}$ and E_{ext} at times that correspond to the velocity snapshots in fig. 13. The horizontal line represents the mean deformation $\mathcal{D}_m$ and the dash-dotted vertical line marks the nondimensional deformation relaxation time $\omega\tau$, where τ is given by eq. (35c). Frame (b) magnifies the part of frame (a) that is our focus.

pushing the dividing streamline into the drop. In line with the instantaneous motion of the interface, the flow direction along the streamlines are from the poles toward the equator. The penetration of the external streamlines into the drop does not last long as they start to retreat back to the ambient fluid shortly (frame (c)). Eventually, the drop reaches the state of maximum deformation (in an absolute sense), where the flow pattern at this state (not shown here) will be quite similar to that of frame (a). After this stage, the rebound half-cycle starts, and as a result, the inner vortices gradually move outward (frames (d) and (e)). Here the poles move away from the drop center while the equator moves toward it, reflecting the fact that the deformation decreases. In line with the motion of the interface, the streamlines cross into the drop from the equator and exit from the poles. Further retreatment of the vortices leads to their disappearance, and as a result, the flow will consist primarily of open-ended streamlines (frames (f)–(h)). As the drop surface moves toward the state of minimum deformation ($\partial\mathcal{D}/\partial t = 0$), and therefore, the deformation-driven flow becomes less dominant, the open-ended streamlines shown in frame (h) will bend further and eventually snap. This leads to formation of closed counter-rotating vortices that cross the drop surface, and are encompassed by a dividing streamline in the ambient (similar to frame (d)). These vortices gradually move into the drop until they are fully confined within the drop, yielding a flow pattern that is exactly the same as that in frame (a). See fig. 11 regarding the evolution of the flow after frame (h).

Figure 11 shows the evolution of the dividing streamline (r_i/a and r_o/a) with time. The dividing streamline is initially incepted inside the drop, close to the center, and then gradually moves outward until it disappears from the sight in the ambient fluid. After a while, a new dividing streamline is incepted in the ambient fluid, essentially marking the start of the quasi-steady state. Defining the residence time of the closed vortices as the fraction of the time during a cycle where the dividing streamline resides inside the drop (*i.e.*, $r_i/a < 1$), it can be said that the flow field is more dominated by the closed vortices than the open-ended streamlines, since the residence time is greater than 50%.

We now turn our attention to the evolution of the flow field under an electric frequency of $\omega = 25\,\text{rad/s}$, corresponding to $\Pi = 1.394$. Here the frequency is above the critical frequency ($\omega_{cr} = 23.199\,\text{rad/s}$), and thus, the mean drop shape is a prolate, but the sense of mean flow circulation remains intact; as before, the mean external flow runs from the poles towards the equator. Fig-

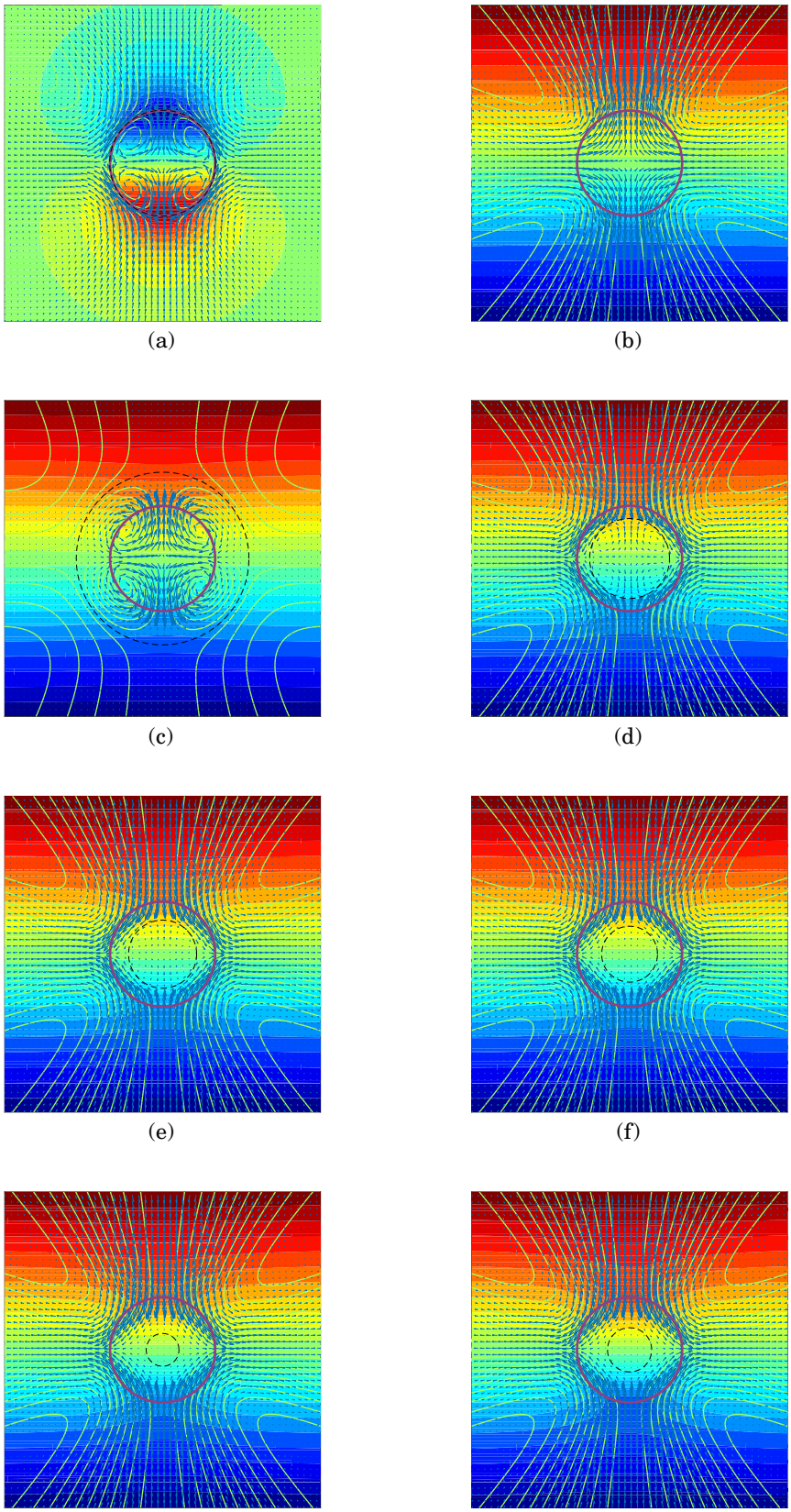

Fig. 13. Vector plot of the velocity field along with the velocity streamlines and contours of the electric potential ϕ for fluid system A and electric field frequency of $\omega = 25\,\mathrm{rad/s}$, corresponding to $\Pi = 1.116$. The frames correspond to the markers in fig. 12.

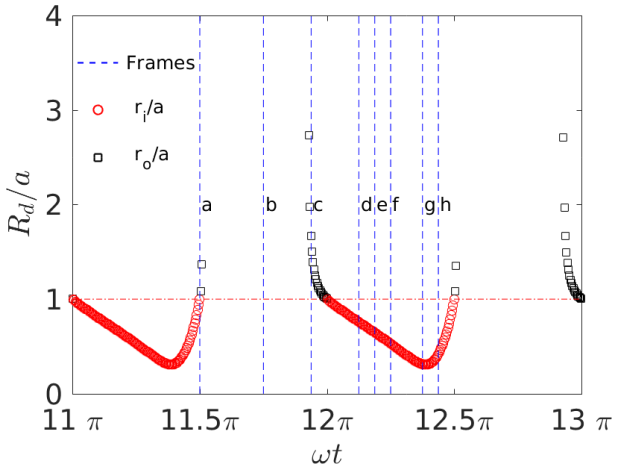

Fig. 14. Evolution of the dividing streamline, r_i/a, r_o/a, with time for fluid system A and electric field frequency of $\omega = 25\,\mathrm{rad/s}$. The dashed vertical lines mark the times of the velocity snapshots in fig. 13.

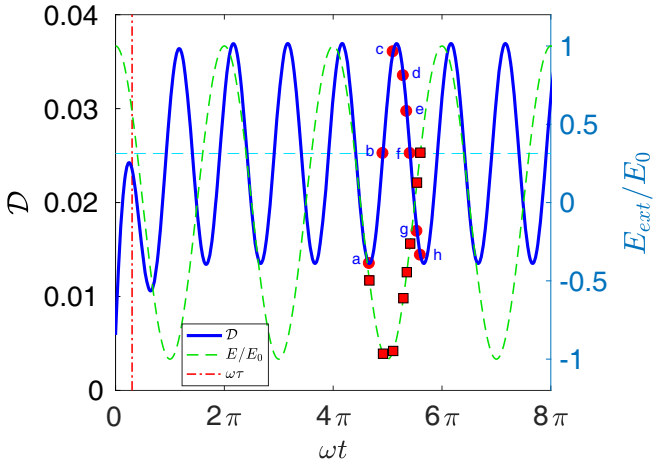

Fig. 15. Evolution of the total deformation $\mathcal{D}$ *versus* nondimensional time ωt for fluid system B and electric field frequency of $\omega = 2\,\mathrm{rad/s}$. The markers identify $\mathcal{D}$ and E_{ext} at times that correspond to the velocity snapshots in fig. 16. The horizontal line represents the mean deformation $\mathcal{D}_m$ and the dash-dotted vertical line marks the nondimensional deformation relaxation time $\omega\tau$, where τ is given by eq. (35c).

ure 12 shows the deformation-time curve; frame (a) shows the evolution of the deformation toward the quasi-steady state, while frame (b) magnifies the part of frame (a) that is our focus. Here the transient period is substantially larger than that in the previous case. Furthermore, the drop oscillates between a prolate ($\mathcal{D} > 0$) and an oblate ($\mathcal{D} < 0$) shape during this period. Figure 13 shows the evolution of the flow field. Frame (a) corresponds to the time of minimum deformation ($\partial\mathcal{D}/\partial t = 0$), and thus, the flow pattern consists of four counter-rotating vortices that fully occupy the drop and are matched with the corresponding vortices in the ambient. Furthermore, no streamline crosses the interface. As soon as the drop moves away from the state of minimum deformation, the inner vortices disappear and are replaced by open-ended streamlines (frame (b)), as can be inferred from fig. 14. As the rate of deformation decreases, a dividing streamline is incepted in the ambient fluid (frame (c)), which gradually moves toward the drop surface and eventually into the drop (frame (d)). As time passes, the dividing streamline moves further into the drop (frames (e)–(g)) until it starts to retreat back (frame (h)). Subsequently, the dividing streamline crosses the drop surface and moves into the ambient fluid until it rapidly disappears (fig. 14). At this point, the process is repeated.

8.1.2 Region **II** (fluid system B)

For fluid systems in this region, the mean behavior of the drop is essentially the same as that of fluid system A with $\omega > \omega_{cr}$. This is due to the fact that according to the deformation-circulation map, the senses of mean deformation and the structure and the sense of mean flow pattern of the both cases are the same; *i.e.*, the mean shape is prolate (at all the field frequencies) and the external streamlines in the mean flow run from the poles toward the equator. We have explored the evolution of the flow field for this fluid system at electric field frequencies of $\omega = 2$ and $\omega = 25\,\mathrm{rad/s}$, corresponding to $\Pi = 0.177$ and $\Pi = 2.213$, respectively.

We first focus on the $\omega = 2\,\mathrm{rad/s}$ case. Here the drop settles to a quasi-steady state in a relatively short time, and the sense of deformation remains intact throughout the process (fig. 15). Figure 16 shows the evolution of the flow field. Frame (a) shows the state of the minimum deformation, where the flow pattern and its direction are the same as the corresponding ones for fluid system A and $\omega > \omega_{cr}$ (fig. 10(a)). Here the dividing streamline moves away from the drop surface and into the ambient until it disappears from the sight in a relatively short time (fig. 17). Subsequently, the flow field will be dominated by open-ended streamlines as seen in frame (b). As time passes, the streamlines are bent until they eventually snap (not shown here), forming closed vortices that cross the drop (frame (c)). These vortices are confined within a dividing streamline that resides in the ambient. From this point onward, the dividing streamline moves toward the drop surface (frame (d)). As time passes it moves into the drop (frames (e) and (f)) until it rapidly disappears (frames (g) and (h)). The flow structure after frame (f) consists of open-ended streamlines only, whose sense of circulation remain intact and tend to reduce the degree of he deformation; note that during the time spanned by frames (e)–(h) the drop is in the rebound half cycle. Overall, compared to the corresponding case for fluid system A (fig. 9), the vortical structure is relatively weak, considering the short residence time of the dividing streamline (fig. 17). This is presumably the result of a stronger deformation-driven fluid flow for this case compared to the previous one.

We now turn our attention to the $\omega = 25\,\mathrm{rad/s}$ case. Figures 18–20 show the results. Here, the transient defor-

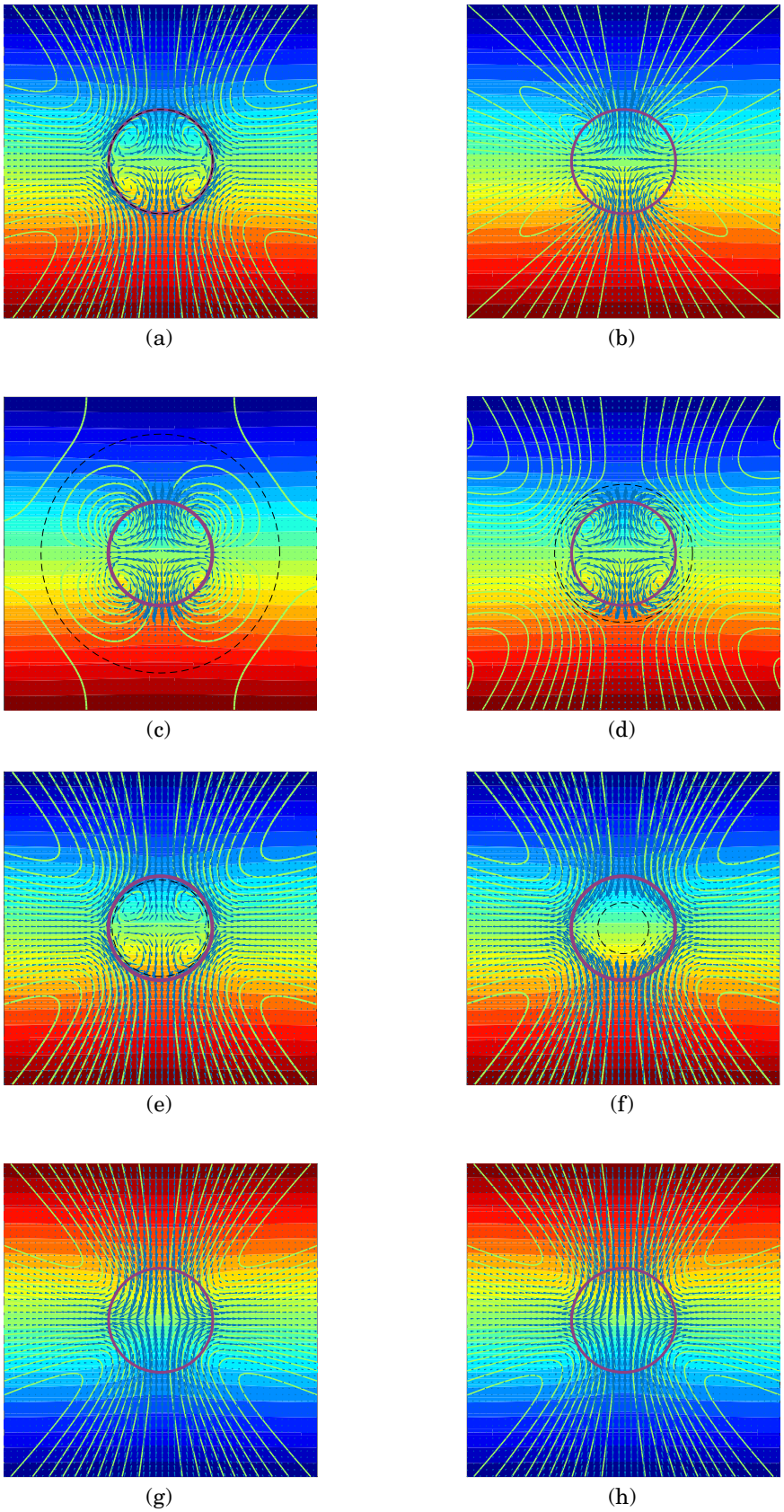

Fig. 16. Vector plot of the velocity field along with the velocity streamlines and contours of the electric potential ϕ for fluid system B and electric field frequency of $\omega = 2\,\mathrm{rad/s}$, corresponding to $\Pi = 0.177$. The frames correspond to the markers in fig. 15.

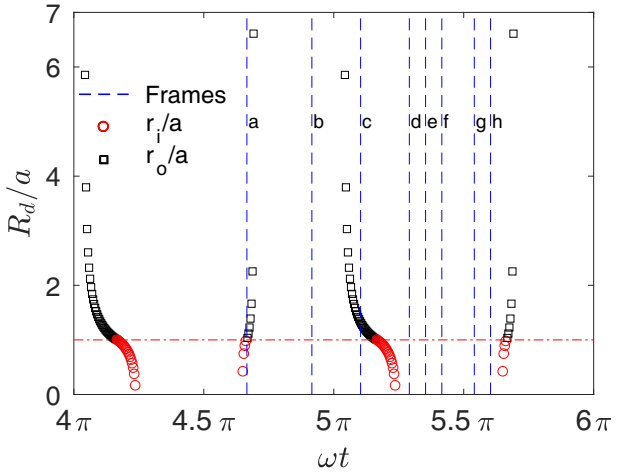

Fig. 17. Evolution of the dividing streamline, r_i/a, r_o/a, with time for fluid system B and electric field frequency of $\omega = 2\,\mathrm{rad/s}$. The dashed vertical lines mark the times of the velocity snapshots in fig. 16.

mation time is about $\omega t_{qs} \approx 20\pi$ (fig. 18), which is substantially larger than that for the previous three cases; $\omega t_{qs} \approx 1.5\pi$ (fig. 9), $\omega t_{qs} \approx 12\pi$ (fig. 12), and $\omega t_{qs} \approx 2\pi$ (fig. 15). This is due to the fact that the mean deformation $\mathcal{D}_m$ for this case is larger than that for the previous cases, and thus, it will take more time for the drop to settle to its quasi-steady state. Note that t_{qs} is discerned from the $\mathcal{D}$-t curves by considering the time that the deformation settles to its quasi-steady state and is generally larger than the relaxation time τ (eq. (35c)). Figure 19 shows the evolution of the velocity field. Frames (a)–(c) and (d)–(h) belong to the deformation and the rebound half cycle, respectively. The transition from open-ended streamlines, which cross into the drop at the equator and exit from the poles and tend to increase the deformation (*i.e.*, making the drop more prolate), to the open-ended streamlines that have the opposite sense of circulation and deformation tendency, takes place rather abruptly shortly after frame (c). Comparison of the results for this case with those for the same fluid at a lower electric frequency, figs. 15–17, suggests that here the residence time of the dividing streamline in the drop is shorter and the vortical structure is weaker. We believe this is due to the more abrupt changes in the senses of flow circulation and drop deformation, which do not let the flow to transition gradually from the deformation half cycle to the rebound half cycle.

8.1.3 Region **III** (fluid system C)

For fluid systems in this region, the mean drop shape is prolate and the mean (external) flow runs from the equator toward the poles. As such, the direction of the mean external flow is the opposite to those in regions **I** and **II**. We explored the evolution of flow field for electric frequency of $\omega = 2\,\mathrm{rad/s}$, corresponding to $\Pi = 1.472$. Here the flow pattern and its evolution (not shown) were similar

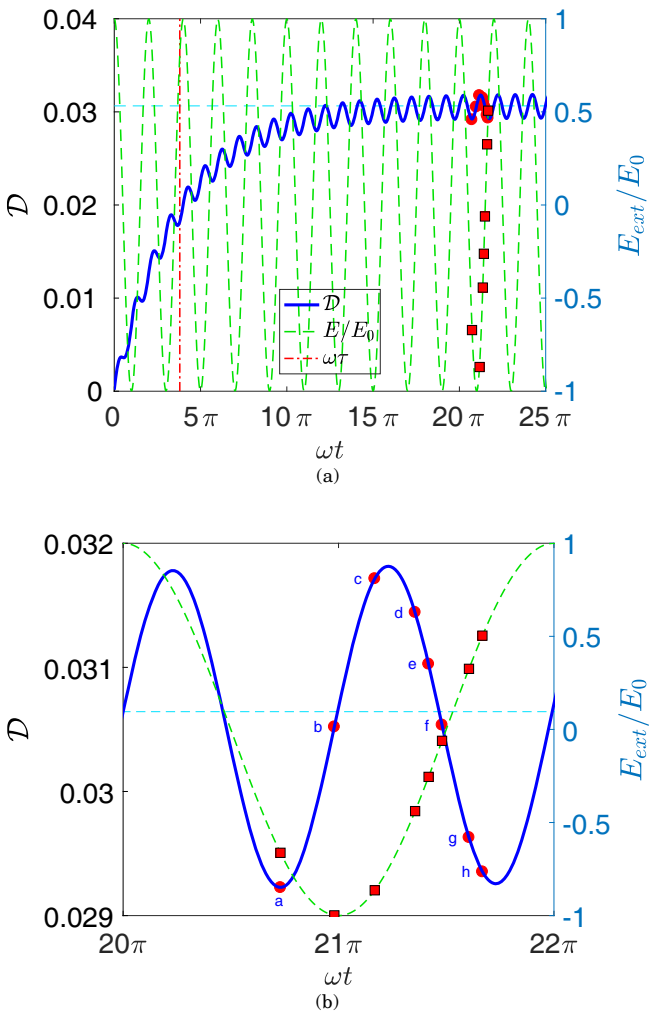

Fig. 18. Evolution of the total deformation $\mathcal{D}$ *vs.* nondimensional time ωt for fluid system B and electric field frequency of $\omega = 25\,\mathrm{rad/s}$ (frame (a)). The markers identify $\mathcal{D}$ and E_{ext} at times that correspond to the velocity snapshots in fig. 19. The horizontal line represents the mean deformation $\mathcal{D}_m$ and the dash-dotted vertical line marks the nondimensional deformation relaxation time $\omega\tau$, where τ is given by eq. (35c). Frame (b) magnifies the part of frame (a) that is our focus.

to the corresponding ones for fluid system B with $\omega = 25$ (fig. 19); the flow field consisted primarily of open-ended streamlines that crossed into the drop from the equator (poles) and exited from the poles (equator). Furthermore, the residence time of the dividing streamlines in the drop was short. Figure 21 shows the evolution of the deformation $\mathcal{D}$ and the dividing streamline, r_i/a and r_o/a for this case.

Since the formation of closed vortices inversely correlates with $\omega(\Pi)$, to explore the possibility of formation of these vortices we reduced the electric field frequency to $\omega = 0.25\,\mathrm{rad/s}$ ($\Pi = 0.184$) and followed the evolution of the flow field. Figures 22–24 show the pertinent results for this case. Here the transient time is relatively short. Furthermore, the mean deformation is larger than that of all

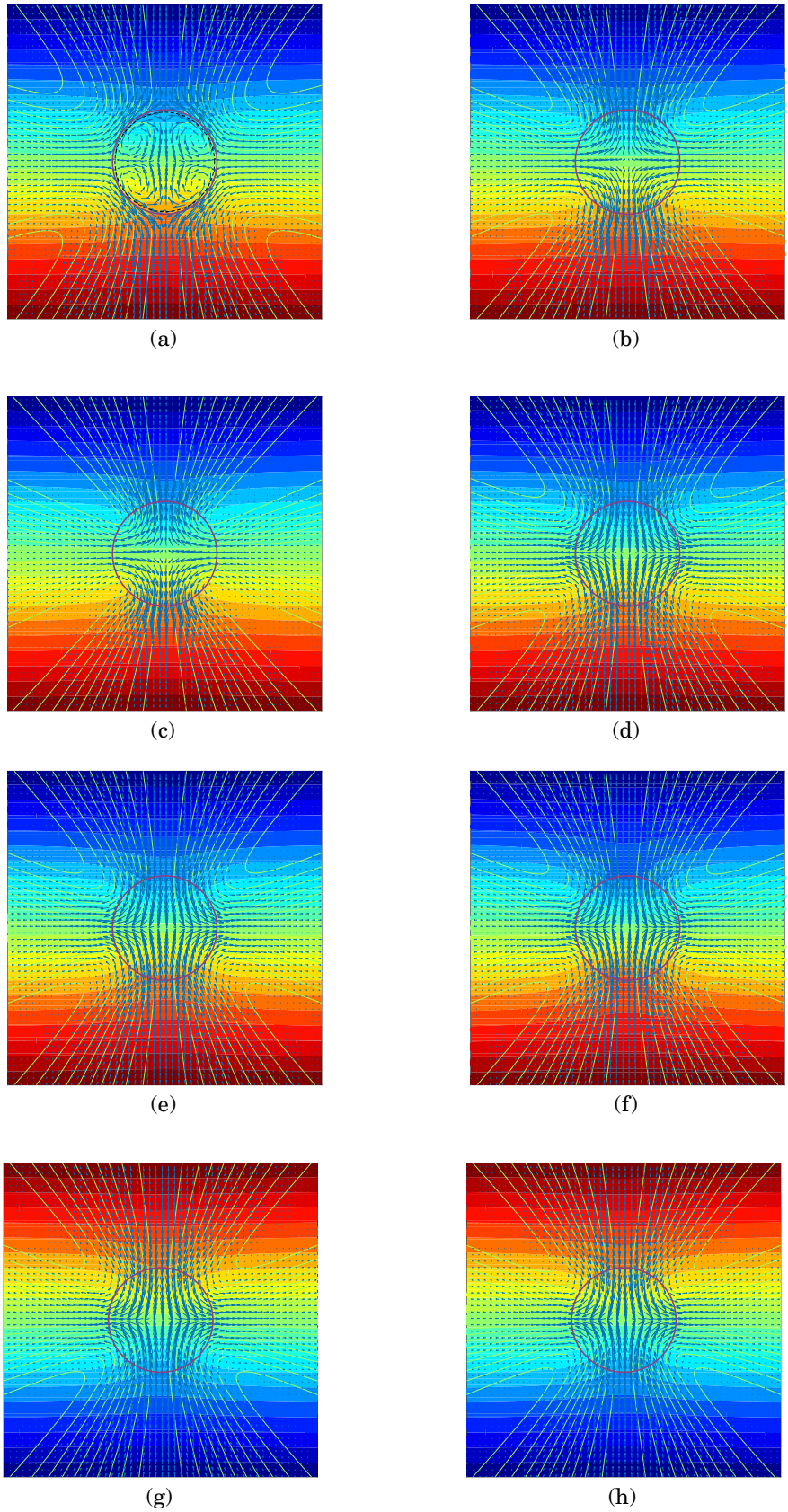

Fig. 19. Vector plot of the velocity field along with the velocity streamlines and contours of the electric potential ϕ for fluid system B and electric field frequency of $\omega = 25\,\mathrm{rad/s}$, corresponding to $\mathit{\Pi} = 2.2135$. The frames correspond to the markers in fig. 18.

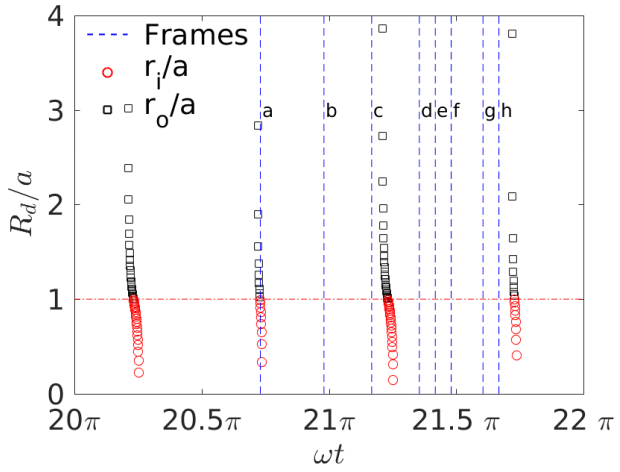

Fig. 20. Evolution of the dividing streamline, r_i/a, r_o/a, with time for fluid system B and electric field frequency of $\omega = 25\,\mathrm{rad/s}$. The dashed vertical lines mark the times of the velocity snapshots in fig. 19.

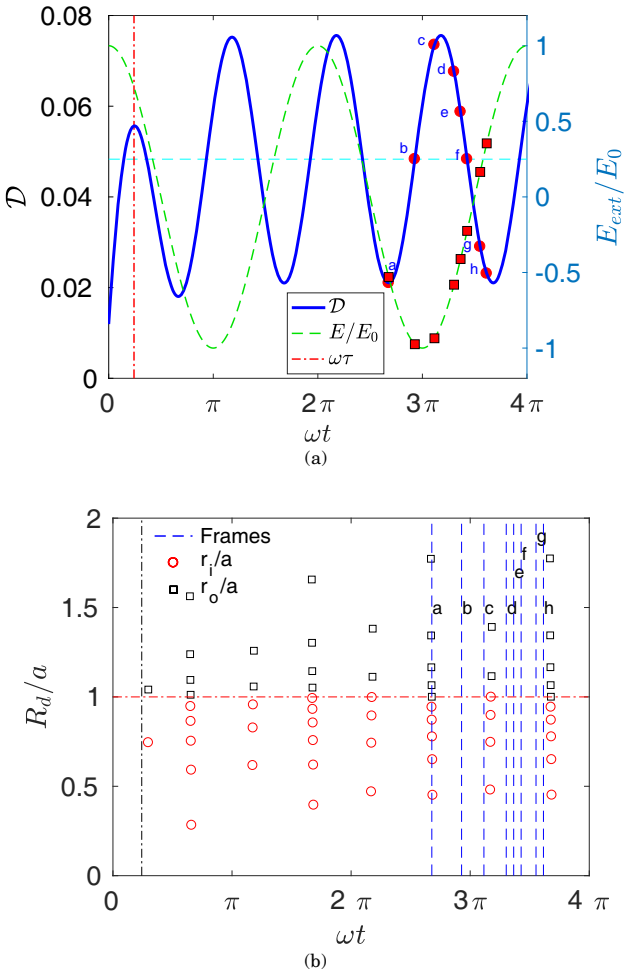

Fig. 21. Evolution of the total deformation $\mathcal{D}$ (frame (a)) and the dividing streamline (frame (b)), r_i/a, r_o/a, *vs.* nondimensional time ωt for fluid system C at electric field frequency of $\omega = 2$. The horizontal line represents the mean deformation $\mathcal{D}_m$ and the dash-dotted vertical line marks the nondimensional deformation relaxation time $\omega\tau$, where τ is given by eq. (35c).

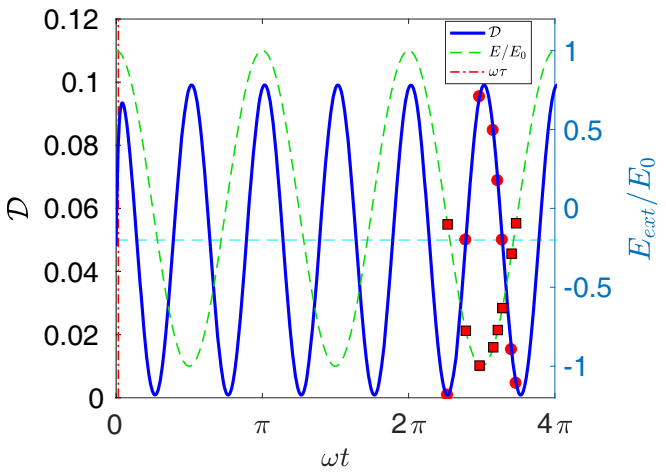

Fig. 22. Evolution of the total deformation $\mathcal{D}$ *vs.* nondimensional time ωt for fluid system C and electric field frequency of $\omega = 0.25\,\mathrm{rad/s}$. The markers identify $\mathcal{D}$ and E_{ext} at times that correspond to the velocity snapshots in fig. 23. The horizontal line represents the mean deformation $\mathcal{D}_m$ and the dash-dotted vertical line marks the nondimensional deformation relaxation time $\omega\tau$, where τ is given by eq. (35c).

the previous cases. The flow field at the state of minimum deformation (frame (a)) comprises counter-rotating vortices that are confined within the drop, and open-ended streamlines that run from the equator toward the poles in the external fluid. Thus, at this stage, the dividing streamline resides at the drop surface. As time passes, the dividing streamline moves into the drop and disappears there rather instantly, as is evident from figs. 23 and 24. The flow field between the times of frames (a) and $(c)^-$ primarily consists of open-ended streamlines, per fig. 24. Here, the superscript "$-$" denotes "shortly before". Shortly before the time of frame (c), a dividing streamline is incepted inside the drop. Frame (c) shows the dividing streamline shortly after the inception, which moves rather rapidly outward (frame (d)) and disappears. The fluid flow during the time period of frames $(d)^+$–$(h)^+$ is mainly dominated by open-ended streamlines. Here, the superscript "$+$" denotes "shortly after". Thus, as opposed to fluid systems in regions **I** and **II**, where the dividing streamline was incepted in the external fluid and moved into the drop, here, the reverse process took place.

9 Relevance of this study to microfluidic applications

The analytical solution presented here was developed assuming small deformation and considering an unbounded domain. However, in many microfluidic applications the drop becomes highly deformed and is typically confined within a microchannel. The question that naturally arises is how the results of this study will be relevant to those circumstances. This question is addressed in the following two paragraphs.

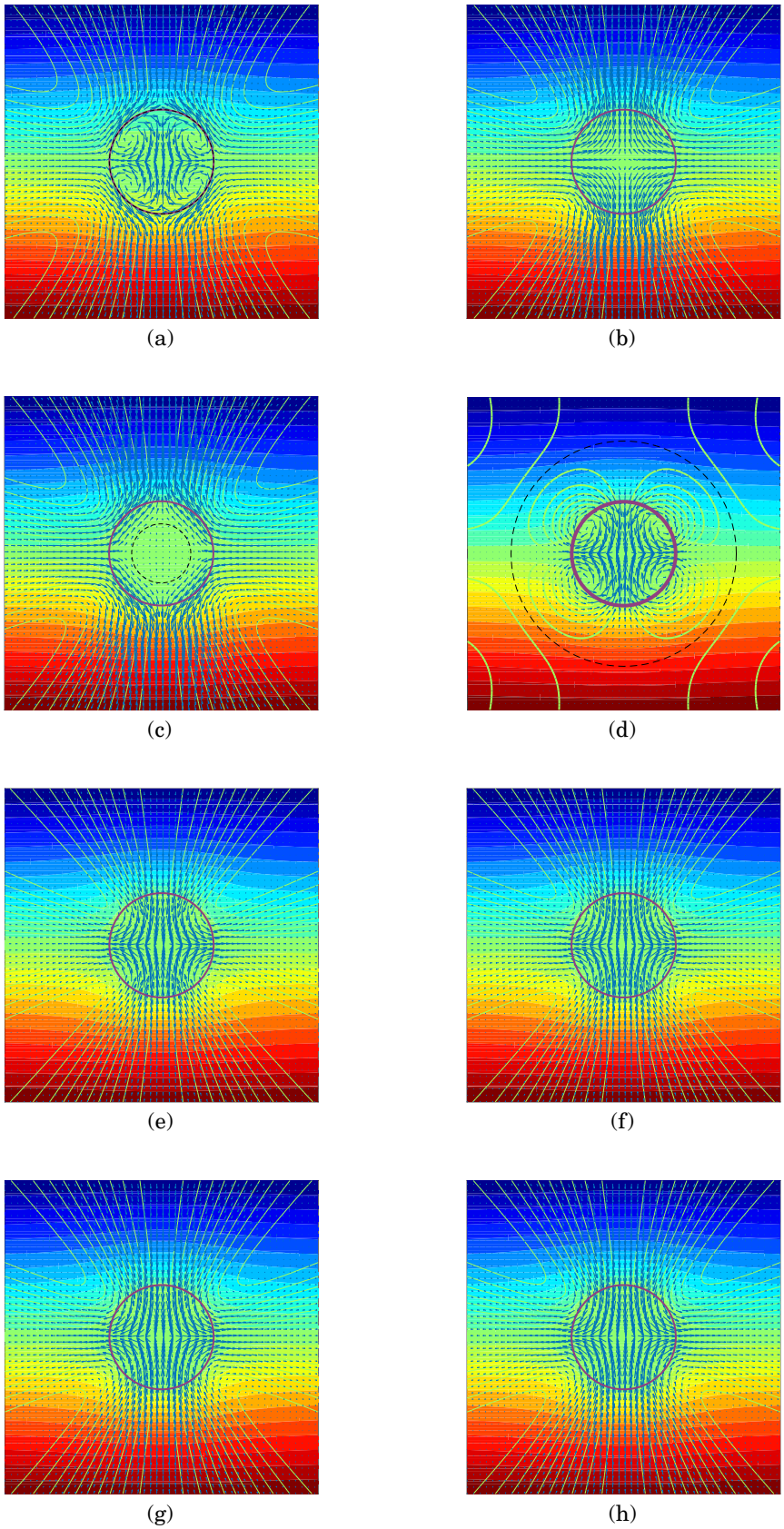

Fig. 23. Vector plot of the velocity field along with the velocity streamlines and contours of the electric potential ϕ for fluid system C and electric field frequency of $\omega = 0.25\,\mathrm{rad/s}$, corresponding to $\mathit{\Pi} = 0.1841$. The frames correspond to the markers in fig. 22.

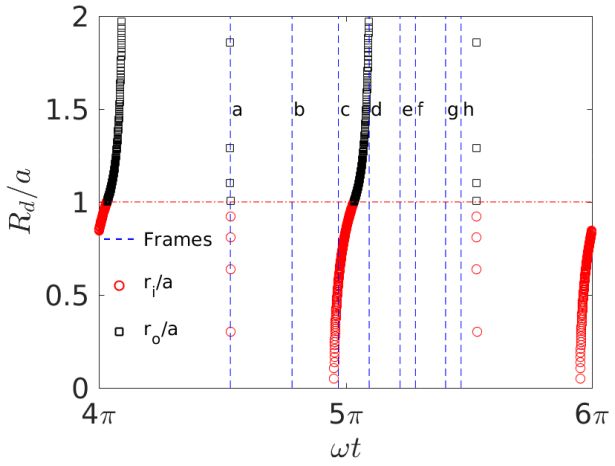

Fig. 24. Evolution of the dividing streamline, r_i/a, r_o/a, with time for fluid system C and electric field frequency of $\omega = 0.25\,\mathrm{rad/s}$. The vertical lines mark the times of the velocity snapshots in fig. 23.

As for the deformation, we remind the reader that this study is concerned with the problems in which the drop deformation is due to application of an external electric field only. For these cases, the current analysis can be useful in the following ways. First, for problems in which the product of the flow capillary number and the characteristic deformation is small, $Ca_f\Phi \ll 1$, the analysis will be readily applicable, since the drop deformation will be small ($\mathcal{D} \ll 1$), per eq. (47). This is achieved in experimental studies with a proper choice of fluid system, noting that Φ is mainly controlled by the ratio of the electric properties of the two fluids. This fact constitutes the basis of the studies of Homsy and collaborators (refs. [14,16], and [17]), who investigated analytically and experimentally transport of heat (or mass) from the drops and chaotic mixing within them considering negligible deformation. Second, the sense of flow circulation is independent of the degree of the drop deformation. Thus, the understanding gained here regarding the flow field and its evolution will be valid for the circumstances in which the drop goes through substantial deformation. It is precisely because of this reason that in DC electric fields the small deformation theory has been used in interpretation of the flow field in computational and experimental studies in which the drop deformation is substantial. See, for example, refs. [26–28], and [29]. Third, the current analysis can be considered a zeroth-order solution in a perturbation series solution of the problem, $\Lambda = \Lambda_0 + \varepsilon\Lambda^1 + O(\varepsilon^2)$, where Λ represents one of the dependent variables (velocity, electric potential, drop deformation, etc.) and ε is a small perturbation parameter; see, for example, ref. [24]. Thus, the solution provided here (Λ_0) can be used to extend the solution to the first order to gain insight into problems in which the drop deformation is tangible; just as Ajayi's extension [30] of Taylor's solution [4] provides us a theoretical basis for instability and break up of drops in a DC electric fields. See, for example, ref. [29] and [31].

As for the confinement effect, two points should be taken into considerations. First, for modest confinement (*i.e.*, manipulation of drops in non-constricted channels), the behavior of the drop will be the same, but the degree of the deformation and the strength of the fluid flow will differ quantitatively from the corresponding ones in an unbounded domain. The direction of the change can be conjectured by predicting the directions of the changes in the tangential and normal electric stresses, as well as the tangential and normal hydrodynamic stresses. Second, for a definitive answer, the current solution can be modified to account for confinement effect by modification of the boundary conditions far away from the drop (*i.e.*, $r \to \infty$) to $r \to b$, where b is the radius of a concentric sphere that encloses the drop; see ref. [32] for a details of the solution in DC electric fields.

10 Conclusions

The fluid flow in and around a liquid drop, driven by an AC electric field, finds relevance in a host of applications aiming to increase the convective effects or fluid mixing. As such, a fundamental understanding about it will help optimize the design and operation of these processes. Unfortunately, the time-periodic structure of the flow field has been largely overlooked so far, leading to some misconceptions about it. To this end, here we explored the evolution of the electrohydrodynamics-driven flow field in and around a liquid drop in a uniform AC electric field ($\mathbf{E}_{ext} = \mathbf{E}_0 \cos\omega t$). The governing equations of the problem were solved analytically in the limit of small deformation and creeping flow regime. It was shown that the mismatch in the dielectric properties of the drop and the ambient fluid leads to the net interfacial tangential and normal electric stresses, $[\![\tau^e_{rr}]\!]$ and $[\![\tau^e_{r\theta}]\!]$, that tend to deform the drop and set the fluid in motion. These stresses comprise a mean (time-independent) and a time-periodic component, $[\![\tau^e_{rr}]\!] = [\![\tau^e_{rr}]\!]_m + [\![\tau^e_{rr}]\!]_{tp}$ and $[\![\tau^e_{r\theta}]\!] = [\![\tau^e_{r\theta}]\!]_m + [\![\tau^e_{r\theta}]\!]_{tp}$. The mean stresses result in a time-exponential fluid flow ψ^{te} and deformation $\mathcal{D}_{te}$, which settle to their corresponding mean values after a relaxation period that is controlled by the time scale of the drop deformation and the viscosities of the fluids. The time-periodic stresses, on the other hand, result in a time-periodic flow ψ^{tp} and deformation $\mathcal{D}^{tp}$ with a frequency of 2ω, which is twice that of the electric field and is the same as the frequency of $[\![\tau^e_{rr}]\!]_{tp}$ and $[\![\tau^e_{r\theta}]\!]_{tp}$. To explore the individual contribution of the mean and the time-periodic stresses, the overall solution was found as the superposition of the solutions resulting from the mean electric stresses ($[\![\tau^e_{rr}]\!]_m$ and $[\![\tau^e_{r\theta}]\!]_m$), the time-periodic tangential electric stress ($[\![\tau^e_{r\theta}]\!]_{tp}$) and the time-periodic normal electric stress ($[\![\tau^e_{rr}]\!]_{tp}$). It was found that the structure and the sense of flow circulation for the mean (time-independent) solution are the same as those in a DC field. However, the sense of mean deformation $\mathcal{D}_m$ is not generally the same as that in a DC field. This information is asserted in the deformation-circulation map (fig. 2). Briefly, for fluid

systems (drop fluid plus ambient fluid) in which the drop deforms to a prolate in a DC electric field ($\mathcal{D}_0 > 0$), the sense of mean deformation remains the same in the corresponding AC field ($\mathcal{D}_m > 0$). On the other hand, for fluid systems in which the drop deforms to an oblate in a DC electric field ($\mathcal{D}_0 < 0$), the sense of the mean deformation may remain the same ($\mathcal{D}_m < 0$) or becomes the opposite ($\mathcal{D}_m > 0$), depending on the field frequency ω being below or above a critical frequency ω_{cr}, respectively.

The evolution of the flow field and drop deformation with time was studied for representative fluid systems at a low and (essentially) a high frequency. The building blocks of the flow pattern at a given time is the open-ended streamlines (open vortices) and the closed vortices. Depending on the strength of the latter being higher or lower than that of the former, the flow field may consist of closed vortices, and hence the "possibility" of a dividing streamline, or may be devoid of them, respectively. Here, by open-ended streamlines we mean those that cross the surface of the drop. At quasi-steady state, the strength of the closed and open vortices can be measured by considering the pertinent velocity scales that were developed in the course of solution; namely, U_m, $U_{T_1}^{tp}$, $U_{T_2}^{tp}$, and U_N^{tp}, corresponding to eqs. (32), (39a), (39d), and (41c), respectively. For this unbounded domain, the external fluid will "always" consist of open-ended streamlines. However, when the rate of the deformation is zero ($\partial\mathcal{D}/\partial t = 0$), none of these streamlines will cross the drop surface. This happens at the extrema of the deformation-time $\mathcal{D}$-t curve. The closed vortices, on the other hand, are formed as a result of the net tangential hydrodynamic stresses $[\![\tau_{r\theta}^h]\!]$. The mean components of the net electric stresses, $[\![\tau_{rr}^e]\!]_m$ and $[\![\tau_{r\theta}^e]\!]_m$, lead to formation of both open-ended streamlines and the closed vortices. However, at sufficiently long time, where $\partial\mathcal{D}_{te}/\partial t = 0$, the flow pattern due to these stresses will be devoid of the open-ended streamlines. The time-periodic net tangential electric stress $[\![\tau_{r\theta}^e]\!]_{tp}$ contributes to both the open-ended streamlines and the closed vortices, while the time-periodic net normal electric stress $[\![\tau_{r\theta}^e]\!]_{tp}$ contributes only to the open-ended streamlines.

In summary, the interplay of the flow patterns generated by the mean and the time-periodic net electric stresses leads to formation and destruction of closed vortices. Judging by the residence time of the dividing streamlines in the drop, the flow field is more dominated by closed vortices for fluid systems chosen from region **I** of the deformation-circulation curve, compared with those from regions **II** and **III**. For regions **I** and **II**, for both $\omega = 2$ and 25 rad/s, the dividing streamline was incepted in the ambient fluid, moved into the drop, and retreated back into the ambient fluid. On the other hand, for region **III**, the dividing streamline was incepted inside the drop and propagated into the ambient fluid. For all the regions, the increase in the frequency led to the destruction of closed vortices, and hence, a decrease in the residence time of the dividing streamlines in the drop.

Finally, a comparison of the results of this study with those of a recent study by ref. [19] will provide an added insight into the problem. It should be noted, however, that only a qualitative comparison can be made since that study was concerned with a two-dimensional drop. Briefly, these authors solved the governing EHD equations numerically, using a front tracking/finite difference scheme. The computational domain was a square box of size $L = 2.5d$ (d being the drop diameter), periodic in the horizontal direction and wall-bounded in the vertical direction. This resulted in an area fraction of 0.1256. There, the drop deformation was appreciable (becoming an ellipse) and the convective effect were not negligible, since $Re_f = 0.5$ and $Ca_f = 0.25$, as opposed to $Re_f \ll 1$ and $Ca_f \ll 1$ in the analytical solution. Inspection of their results shows that, for all the fluid systems considered, the senses of their mean drop deformation and the mean flow circulation are in line with the theoretical predictions presented here. This reinforces the fact that the sense of mean drop deformation and flow circulation is not altered by the degree of the drop deformation. A major qualitative difference between the two flow fields, however, exists with respect to the shape of the streamlines that extend into the external fluid. Whereas in the current study the flow field very often consisted of the open-ended streamlines, which approached the drop along the equator (the poles) and departed along the poles (equator), in the numerical simulations these streamlines were replaced with closed curves. This is due to the confinement effect, which is present in the numerical simulations, but is absent in the current study. Similarly, the evolution of the flow field in the numerical study did not show some of the fascinating flow structures that were observed in the present study, since the growth of the dividing streamline in the external flow was impeded due to the confinement effects. It should be noted, however, that if the computational domain in the numerical simulations had been sufficiently large (*i.e.*, $L \gtrapprox 5d$), the numerical flow fields would have matched the analytical ones more closely.

Appendix A. Solution of momentum equation for flow driven by $[\![\tau_{rr}^e]\!]_m$ and $[\![\tau_{r\theta}^e]\!]_m$

In what follows, subscript m denotes mean (time-independent) parameters, while subscript or superscript te is used to denote time-exponential parameters. Here, eq. (29) is rewritten as

$$\psi_i = (A_i^{te} r^3 + B_i^{te} r^5) \sin^2\theta \cos\theta, \tag{A.1a}$$

$$\psi_o = (A_o^{te} r^{-2} + B_o^{te}) \sin^2\theta \cos\theta, \tag{A.1b}$$

to customize it for the present solution. The unknown coefficients in eq. (A.1) are determined from the interfacial jump conditions. The jump conditions are expressed in terms of the velocity field, considering $\mathbf{u}_i^{te} = (u_{r_i}^{te}, u_{\theta_i}^{te})$ and $\mathbf{u}_o^{te} = (u_{r_o}^{te}, u_{\theta_i}^{te})$. In the process of application of the jump conditions, the drop shape function ξ_{te} and the curvature κ_{te} are needed. For this zeroth-order solution, the structure of the shape function can be discerned from the normal stress balance [24], which suggests $\xi_{te}(t) = a[1 + (2/3)\mathcal{D}_{te}(t)(3\cos^2\theta - 1)]$. Using the

suggested shape function, the curvature is found to be $\kappa_{te} = 2/a + (8\mathcal{D}_{te}/3a)(3\cos^2\theta - 1)$. The net hydrodynamic stresses, $[\![\tau^h_{r\theta}]\!]_{te}$, $[\![\tau^h_{rr}]\!]_{te}$, and the pressure jump, $[\![p]\!]_{te}$, are needed and are calculated by integration of $-\nabla p^{te} + \mu\nabla^2\mathbf{u}^{te} = \mathbf{0}$ (which is the customized form of eq. (10)), in conjunction with eq. (A.1).

The following jump conditions apply:

I) Continuity of the tangential velocity, $u^{te}_{\theta_o} = u^{te}_{\theta_i}$ at $r = a$.
II) Continuity of the radial (normal) velocity, $u^{te}_{r_o} = u^{te}_{r_i} = \partial\xi_{te}/\partial t$ at $r = a$. Note that this boundary condition results in two equations.
III) Tangential force balance, $[\![\tau^e_{r\theta}]\!]_m + [\![\tau^h_{r\theta}]\!]_{te} = 0$.
IV) Normal force balance, $[\![\tau^e_{rr}]\!]_m + [\![\tau^h_{rr}]\!]_{te} - [\![p]\!]_{te} = \gamma\kappa_{te}$.

Jump conditions I)–IV) constitute five equations for the five unknowns, A^{te}_i, B^{te}_i, A^{te}_o, B^{te}_o, and $\mathcal{D}_{te}$, leading to

$$3aA^{te}_i + 5a^3B^{te}_i + 2a^{-4}A^{te}_o = 0, \tag{A.2a}$$

$$A^{te}_i + a^2B^{te}_i = \frac{2}{3}\frac{\partial\mathcal{D}_{te}}{\partial t}, \tag{A.2b}$$

$$a^{-4}A^{te}_o + a^{-2}B^{te}_o = \frac{2}{3}a\frac{\partial\mathcal{D}_{te}}{\partial t}, \tag{A.2c}$$

$$\widetilde{[\![\tau^e_{r\theta}]\!]} - \mu_o\left(8a^{-5}A^{te}_o + 3a^{-3}B^{te}_o\right) + \mu_i(3A^{te}_i + 8a^2B^{te}_i) = 0, \tag{A.2d}$$

$$\widetilde{[\![\tau^e_{rr}]\!]} - 3\mu_o\left(8a^{-5}A^{te}_o + 6a^{-3}B^{te}_o\right) + 3\mu_i\left(-2A^{te}_i + a^2B^{te}_i\right) = \frac{8\gamma\mathcal{D}_{te}}{a}. \tag{A.2e}$$

Here, $\widetilde{[\![\tau^e_{r\theta}]\!]}$ and $\widetilde{[\![\tau^e_{r\theta}]\!]}$ are the coefficients of $\cos^2\theta$ and $\sin 2\theta$ in eq. (23a) and (24a), respectively. Notice that since the jump conditions should be valid at any point at the drop surface, only the coefficients of $\cos^2\theta$ terms in the normal force balance equation are retained.

Solution of eq. (A.2) yields A^{te}_i, B^{te}_i, A^{te}_o, and B^{te}_o in terms of the parameters of the problem and the rate of deformation $\partial\mathcal{D}_{te}/\partial t$

$$A^{te}_i = \frac{1}{5(\widetilde{\mu}+1)}\left(\frac{16\widetilde{\mu}+19}{3}\frac{\partial\mathcal{D}_{te}}{\partial t} + \frac{\widetilde{[\![\tau^e_{r\theta}]\!]}}{\mu_o}\right), \tag{A.3a}$$

$$B^{te}_i = \frac{1}{5(\widetilde{\mu}+1)a^2}\left(-(2\widetilde{\mu}+3)\frac{\partial\mathcal{D}_{te}}{\partial t} - \frac{\widetilde{[\![\tau^e_{r\theta}]\!]}}{\mu_o}\right), \tag{A.3b}$$

$$A^{te}_o = \frac{a^5}{5(\widetilde{\mu}+1)}\left(-(3\widetilde{\mu}+2)\frac{\partial\mathcal{D}_{te}}{\partial t} + \frac{\widetilde{[\![\tau^e_{r\theta}]\!]}}{\mu_o}\right), \tag{A.3c}$$

$$B^{te}_o = \frac{a^3}{5(\widetilde{\mu}+1)}\left(\frac{19\widetilde{\mu}+16}{3}\frac{\partial\mathcal{D}_{te}}{\partial t} - \frac{\widetilde{[\![\tau^e_{r\theta}]\!]}}{\mu_o}\right), \tag{A.3d}$$

where

$$\tau\frac{\partial\mathcal{D}_{te}}{\partial t} + \mathcal{D}_{te} = \underbrace{\frac{a}{8\gamma}\left(\widetilde{[\![\tau^e_{rr}]\!]} - \frac{3}{5}\frac{3\widetilde{\mu}+2}{\widetilde{\mu}+1}\widetilde{[\![\tau^e_{r\theta}]\!]}\right)}_{\mathcal{D}_m} \tag{A.4}$$

determines the deformation $\mathcal{D}_{te}$. Here τ is the characteristic time scale that governs the dynamics. Solution of eq. (A.4) leads to $\mathcal{D}_{te}$, eq. (34), which suggests that the drop deformation settles monotonically to its steady-state value. Notice that the right hand side of eq. (A.4) is the time-independent deformation $\mathcal{D}_m$ as given in eq. (35a). Once $\mathcal{D}_{te}$ is determined, the unknown coefficients of the streamfunction are found from eq. (A.3), leading to determination of streamfunction, per eq. (31).

Appendix B. Solution of momentum equation for flow driven by $[\![\tau^e_{r\theta}]\!]_{tp}$

In what follows, subscript or superscript tp denotes time-periodic parameters, while subscript or superscript T stands for tangential, which is used to signify that the net electric tangential stress $[\![\tau^e_{r\theta}]\!]_{tp}$ is the driver. For time-periodic flows it is more convenient to use "the method of complex variables" by considering a complex streamfunction $\psi^{tp\prime}(r,\theta,t) = \psi^{tp*}(r,\theta)e^{2i\omega t}$ whose real part $\psi^{tp} = \mathbb{R}\mathrm{e}(\psi^{tp\prime})$ constitutes the solution, $\psi^{tp*}(r,\theta)$ being the time-independent complex streamfunction. Accordingly, eq. (29) can be rewritten as

$$\psi^{tp\,*}_{i_T} = \left(A^{tp\,*}_{i_T}r^3 + B^{tp\,*}_{i_T}r^5\right)\sin^2\theta\cos\theta, \tag{B.1a}$$

$$\psi^{tp\,*}_{o_T} = \left(A^{tp\,*}_{o_T}r^{-2} + B^{tp\,*}_{o_T}\right)\sin^2\theta\cos\theta, \tag{B.1b}$$

in terms of the time-independent complex coefficients.

Here we express the jump conditions in terms of the velocity field, considering the complex velocities as $u^{T\,\prime}_{r_i} = u^{T\,*}_{r_i}e^{2i\omega t}$ and $u^{T\,\prime}_{\theta_i} = u^{T\,*}_{\theta_i}e^{2i\omega t}$, where $u^T_{r_i} = \mathbb{R}\mathrm{e}(u^{T\,\prime}_{r_i})$ and $u^T_{\theta_i} = \mathbb{R}\mathrm{e}(u^{T\,\prime}_{\theta_i})$. Furthermore, using the same argument as in appendix A the drop shape function and curvature are found to be $\xi^{tp}_T(t) = (2/3)a\mathcal{D}^{tp}_T(t)(3\cos^2\theta - 1)$ and $\kappa^{tp}_T(t) = (8\mathcal{D}^{tp}_T(t)/3a)(3\cos^2\theta - 1)$. In a manner similar to the definition of complex streamfunction, we consider $\xi^{tp}_T = \mathbb{R}\mathrm{e}(\xi^{tp\prime}_T)$, where $\xi^{tp\prime}_T = \xi^{tp*}_T e^{2i\omega t}$, $\kappa^{tp}_T = \mathbb{R}\mathrm{e}(\kappa^{tp\prime}_T)$, where $\kappa^{tp\prime}_T = \kappa_{tp}{}^* e^{2i\omega t}$, and $[\![Q]\!] = \mathbb{R}\mathrm{e}([\![Q]\!]')$, where $[\![Q]\!]' = [\![Q]\!]^* e^{2i\omega t}$. Here, the double bracket denotes the jump in a typical parameter Q (outside minus inside) across the interface.

The following jump conditions apply:

I) Continuity of the tangential velocity, $u^T_{\theta_o} = u^T_{\theta_i}$ at $r = a$, which leads to $u^{T\,*}_{\theta_i} = u^{T\,*}_{\theta_o}$ at $r = a$.
II) Continuity of the radial (normal) velocity, $u^T_{r_i} = u^T_{r_o} = \partial\xi^{tp}_T/\partial t$ at $r = a$, which leads to $u^{T\,*}_{r_i} = u^{T\,*}_{r_o} = 2i\omega\xi^{tp*}_T$ at $r = a$. Note that this boundary condition results in two equations.
III) Tangential force balance, $[\![\tau^e_{r\theta}]\!]_{tp} + [\![\tau^h_{r\theta}]\!]^T_{tp} = 0$, which leads to $[\![\tau^e_{r\theta}]\!]^*_{tp} + [\![\tau^h_{r\theta}]\!]^{T\,*}_{tp} = 0$.
IV) Normal force balance, $[\![\tau^h_{rr}]\!]^T_{tp} - [\![p]\!]^T_{tp} = \gamma\kappa^{tp}_T$, which leads to $[\![\tau^h_{rr}]\!]^{T\,*}_{tp} - [\![p]\!]^{T\,*}_{tp} = \gamma\kappa T_{tp}{}^*$.

Jump conditions I)–IV) constitute five equations for the five unknowns, $A_{i_T}^{tp\,*}$, $B_{i_T}^{tp\,*}$, $A_{o_T}^{tp\,*}$, $B_{o_T}^{tp\,*}$, and $\mathcal{D}_T^*$, leading to

$$3aA_{i_T}^{tp\,*} + 5a^3B_{i_T}^{tp\,*} + 2a^{-4}A_{o_T}^{tp\,*} = 0, \tag{B.2a}$$

$$A_{i_T}^{tp\,*} + a^2B_{i_T}^{tp\,*} = \frac{4}{3}\omega i\mathcal{D}_T^{tp*}, \tag{B.2b}$$

$$a^{-4}A_{o_T}^{tp\,*} + a^{-2}B_{o_T}^{tp\,*} = \frac{4}{3}a\omega i\mathcal{D}_T^{tp*}, \tag{B.2c}$$

$$\frac{9\epsilon_o E_0^2(\widetilde{\epsilon}-\widetilde{\sigma})}{4}F_\theta^* - \mu_o\left(8a^{-5}A_{o_T}^{tp\,*} + 3a^{-3}B_{o_T}^{tp\,*}\right) + \mu_i\left(3A_{i_T}^{tp\,*} + 8a^2B_{i_T}^{tp\,*}\right) = 0, \tag{B.2d}$$

$$-3\mu_o\left(8a^{-5}A_{o_T}^{tp\,*} + 6a^{-3}B_{o_T}^{tp\,*}\right) + 3\mu_i\left(-2A_{i_T}^{tp\,*} + a^2B_{i_T}^{tp\,*}\right) = \frac{8\gamma\mathcal{D}_T^{tp*}}{a}. \tag{B.2e}$$

Here we first use jump conditions (B.2a)–(B.2c) and (B.2e) to determine $A_{i_T}^{tp\,*}$, $B_{i_T}^{tp\,*}$, $A_{o_T}^{tp\,*}$, and $B_{o_T}^{tp\,*}$ in terms of $\mathcal{D}_T^*$ and then substitute for these coefficients in (B.2d) to find $\mathcal{D}_T^*$. This yields

$$\mathcal{D}_T^{tp*} = \frac{9}{32}Ca_f d_T^*, \tag{B.3a}$$

$$d_T^* = \frac{-\lambda_1(\widetilde{\epsilon}-\widetilde{\sigma})F_\theta^*}{1+iCa_\omega\lambda_2}, \tag{B.3b}$$

$$\lambda_1 = \frac{3(3\widetilde{\mu}+2)}{5(\widetilde{\mu}+1)}, \qquad \lambda_2 = \frac{(19\widetilde{\mu}+16)(2\widetilde{\mu}+3)}{20(\widetilde{\mu}+1)}, \tag{B.3c}$$

and

$$A_{i_T}^{tp\,*} = C_{1_T}^* + C_{2_T}^*(16\widetilde{\mu}+19), \tag{B.4a}$$

$$B_{i_T}^{tp\,*} = -a^{-2}\left[C_{1_T}^* + 3C_{2_T}^*(2\widetilde{\mu}+3)\right], \tag{B.4b}$$

$$A_{o_T}^{tp\,*} = a^5\left[C_{1_T}^* - 3C_{2_T}^*(3\widetilde{\mu}+2)\right], \tag{B.4c}$$

$$B_{o_T}^{tp\,*} = -a^3\left[C_{1_T}^* - C_{2_T}^*(19\widetilde{\mu}+16)\right], \tag{B.4d}$$

where

$$C_{1_T}^* = \frac{9\epsilon_o E_0^2(\widetilde{\epsilon}-\widetilde{\sigma})}{20\mu_o(\widetilde{\mu}+1)}F_\theta^*, \qquad C_{2_T}^* = \frac{2\mathcal{D}_T^{tp*}\omega i}{15(\widetilde{\mu}+1)}. \tag{B.5}$$

Subsequently, the streamfunction and the drop deformation are determined as given in eqs. (38) and (40), using the following expressions:

$$d_T^* = d_{T_R} + id_{T_I}, \qquad |d_T^*| = \sqrt{d_{T_R}^2 + d_{T_I}^2}, \tag{B.6a}$$

$$d_{T_R} = \frac{d_{T_{R_1}} - d_{T_{R_2}}}{\Lambda^2(1+Ca_\omega^2\lambda_2^2)}, \qquad d_{T_I} = -\frac{d_{T_{I_1}} + d_{T_{I_2}}}{\Lambda^2(1+Ca_\omega^2\lambda_2^2)}, \tag{B.6b}$$

where

$$d_{T_{R_1}} = \lambda_1(\widetilde{\sigma}-\widetilde{\epsilon})\left[(\widetilde{\sigma}+2)^2 + \Pi^2(2\widetilde{\sigma}-\widetilde{\epsilon}+2)(\widetilde{\epsilon}+2)\right], \tag{B.7a}$$

$$d_{T_{R_2}} = \lambda_1(\widetilde{\sigma}-\widetilde{\epsilon})Ca_\omega\Pi\lambda_2[2\widetilde{\sigma}\widetilde{\epsilon} + 4\widetilde{\epsilon} + 4 - \widetilde{\sigma}^2 + \Pi^2(\widetilde{\epsilon}+2)^2], \tag{B.7b}$$

$$d_{T_{I_1}} = \lambda_1(\widetilde{\sigma}-\widetilde{\epsilon})[-\Pi(\widetilde{\sigma}+2)(\widetilde{\sigma}-2\widetilde{\epsilon}-2) + \Pi^3(\widetilde{\epsilon}+2)^2], \tag{B.7c}$$

$$d_{T_{I_2}} = \lambda_1(\widetilde{\sigma}-\widetilde{\epsilon})Ca_\omega\lambda_2[(\widetilde{\sigma}+2)^2 + \Pi^2(2\widetilde{\sigma}-\widetilde{\epsilon}+2)(\widetilde{\epsilon}+2)]. \tag{B.7d}$$

Appendix C. Solution of momentum equation for flow driven by $[\![\tau_{rr}^e]\!]_{tp}$

In what follows, subscript or superscript *tp* denotes time-periodic parameters, while subscript or superscript *N* stands for normal and is used to signify that the net electric normal stress $[\![\tau_{rr}^e]\!]_{tp}$ is the driver. We take the same approach as that taken in appendix B. Accordingly, the suggested solution is

$$\psi_{i_N}^{tp\,*} = \left(A_{i_N}^{tp\,*}r^3 + B_{i_N}^{tp\,*}r^5\right)\sin^2\theta\cos\theta, \tag{C.1a}$$

$$\psi_{o_N}^{tp\,*} = \left(A_{o_N}^{tp\,*}r^{-2} + B_{o_N}^{tp\,*}\right)\sin^2\theta\cos\theta. \tag{C.1b}$$

Here $\psi_N^{tp*}(r,\theta)$ is the time-independent complex streamfunction, which is related to the real solution through $\psi_N^{tp} = \mathbb{R}\mathrm{e}(\psi_N^{tp\prime})$, $\psi_N^{tp\prime}(r,\theta,t) = \psi_N^{tp*}(r,\theta)e^{2i\omega t}$ being the complex streamfunction. As in appendix B, the jump conditions are expressed in terms of the velocity field, considering the complex velocities as $u_{r_i}^{N\prime} = u_{r_i}^{N*}e^{2i\omega t}$ and $u_{\theta_i}^{N\prime} = u_{\theta_i}^{N*}e^{2i\omega t}$, where $u_{r_i}^N = \mathbb{R}\mathrm{e}(u_{r_i}^{N\prime})$ and $u_{\theta_i}^N = \mathbb{R}\mathrm{e}(u_{\theta_i}^{N\prime})$. Here, the shape factor and the curvature are $\xi_N^{tp}(t) = (2/3)a\mathcal{D}_N^{tp}(t)(3\cos^2\theta - 1)$ and $\kappa_N^{tp}(t) = (8\mathcal{D}_N^{tp}(t)/3a)(3\cos^2\theta - 1)$; as before $\xi_N^{tp} = \mathbb{R}\mathrm{e}(\xi_N^{tp\prime})$ and $\kappa_N^{tp} = \mathbb{R}\mathrm{e}(\kappa_N^{tp\prime})$, where $\xi_N^{tp\prime} = \xi_N^{tp*}e^{2i\omega t}$ and $\kappa_N^{tp\prime} = \kappa_{tp}{}^*e^{2i\omega t}$.

The following jump conditions apply:

I) Continuity of the tangential velocity, $u_{\theta_i}^N = u_{\theta_o}^N$ at $r = a$, which leads to $u_{\theta_i}^{N*} = u_{\theta_o}^{N*}$ at $r = a$.

II) Continuity of the radial (normal) velocity, $u_{r_i}^N = u_{r_o}^N = \partial\xi_N^{tp}/\partial t$ at $r = a$, which leads to $u_{r_i}^{N*} = u_{r_o}^{N*} = 2i\omega\xi_N^{tp*}$ at $r = a$.

III) Tangential force balance, $[\![\tau_{r\theta}^h]\!]_{tp}^N = 0$, which leads to $[\![\tau_{r\theta}^h]\!]_{tp}^{N*} = 0$.

IV) Normal force balance, $[\![\tau_{rr}^e]\!]_{tp} + [\![\tau_{rr}^h]\!]_{tp}^N - [\![p]\!]_{tp}^N = \gamma\kappa_N^{tp}$, which leads to $[\![\tau_{rr}^e]\!]_{tp}^* + [\![\tau_{rr}^h]\!]_{tp}^{N*} - [\![p]\!]_{tp}^{N*} = \gamma\kappa_N^{tp*}$.

Jump conditions I)–IV) constitute five equations for the five unknowns, $A_{i_N}^{tp\,*}$, $B_{i_N}^{tp\,*}$, $A_{o_N}^{tp\,*}$, $B_{o_N}^{tp\,*}$, and $\mathcal{D}_N^*$,

leading to

$$3aA_{i_N}^{tp\,*} + 2a^{-4}A_{o_N}^{tp\,*} + 5a^3B_{i_N}^{tp\,*} = 0, \tag{C.2a}$$

$$A_{i_N}^{tp\,*} + a^2B_{i_N}^{tp\,*} = \frac{4}{3}\omega i\mathcal{D}_N^{tp*}, \tag{C.2b}$$

$$a^{-4}A_{o_N}^{tp\,*} + a^{-2}B_{o_N}^{tp\,*} = \frac{4}{3}a\omega i\mathcal{D}_N^{tp*}, \tag{C.2c}$$

$$-\mu_o\left(8a^{-5}A_{o_N}^{tp\,*} + 3a^{-3}B_{o_N}^{tp\,*}\right) + \mu_i\left(3A_{i_N}^{tp\,*} + 8a^2B_{i_N}^{tp\,*}\right) = 0, \tag{C.2d}$$

$$\frac{9\epsilon_o E_0^2}{4}F_r^* - 3\mu_o\left(8a^{-5}A_{o_N}^{tp\,*} + 6a^{-3}B_{o_N}^{tp\,*}\right) + 3\mu_i\left(-2A_{i_N}^{tp\,*} + a^2B_{i_N}^{tp\,*}\right) = \frac{8\gamma\mathcal{D}_N^{tp*}}{a}. \tag{C.2e}$$

Here we first use jump conditions (C.2a)–(C.2d) to determine $A_{i_N}^{tp\,*}$, $B_{i_N}^{tp\,*}$, $A_{o_N}^{tp\,*}$, and $B_{o_N}^{tp\,*}$ in terms of $\mathcal{D}_N^*$, and then substitute for these coefficients in jump condition (C.2e) to find $\mathcal{D}_N^*$. This yields

$$\mathcal{D}_N^{tp*} = \frac{9}{32}Ca_f d_N^*, \tag{C.3a}$$

$$d_N^* = \frac{F_r^*}{1 + iCa_\omega\lambda_2}, \tag{C.3b}$$

and

$$A_{i_N}^{tp\,*} = C_N^*(16\widetilde{\mu} + 19), \tag{C.4a}$$

$$B_{i_N}^{tp\,*} = -3a^{-2}C_N^*(2\widetilde{\mu} + 3), \tag{C.4b}$$

$$A_{o_N}^{tp\,*} = -3a^5C_N^*(3\widetilde{\mu} + 2), \tag{C.4c}$$

$$B_{o_N}^{tp\,*} = a^3C_N^*(19\widetilde{\mu} + 16), \tag{C.4d}$$

where

$$C_N^* = \frac{2\mathcal{D}_N^{tp*}\omega i}{15(\widetilde{\mu} + 1)}. \tag{C.5}$$

Subsequently, the streamfunction and the drop deformation are determined as given in eqs. (41) and (42), using the following expressions:

$$d_N^* = d_{N_R} + id_{N_I}, \qquad |d_N^*| = \sqrt{d_{N_R}^2 + d_{N_I}^2}, \tag{C.6a}$$

$$d_{N_R} = \frac{d_{N_{R_1}} + d_{N_{R_2}} + d_{N_{R_3}} - d_{N_{R_4}}}{\Lambda^2(1 + Ca_\omega^2\lambda_2^2)},$$

$$d_{N_I} = -\frac{d_{N_{I_1}} + d_{N_{I_2}} + d_{N_{I_3}} + d_{N_{I_4}}}{\Lambda^2(1 + Ca_\omega^2\lambda_2^2)}, \tag{C.6b}$$

where

$$d_{N_{R_1}} = (\widetilde{\sigma} + 2)^2(\widetilde{\sigma}^2 - 2\widetilde{\epsilon} + 1), \tag{C.7a}$$

$$d_{N_{R_2}} = \Pi^2\left[-5\widetilde{\sigma}^2 + 4\widetilde{\sigma} + 6\widetilde{\epsilon}(\widetilde{\sigma}^2 + 2\widetilde{\sigma} - 2) + (2\widetilde{\sigma}^2 - 4\widetilde{\sigma} - 13)\widetilde{\epsilon}^2 + 2\widetilde{\epsilon}^3 + 8\right], \tag{C.7b}$$

$$d_{N_{R_3}} = \Pi^4(\widetilde{\epsilon}^2 + \widetilde{\epsilon} - 2)^2, \tag{C.7c}$$

$$d_{N_{R_4}} = (\widetilde{\sigma} - \widetilde{\epsilon})Ca_\omega\Pi\lambda_2\left[-4 + 8\widetilde{\epsilon} + 6\widetilde{\sigma} + 4\widetilde{\sigma}\widetilde{\epsilon} + 4\widetilde{\sigma}^2 + 2\Pi^2(\widetilde{\epsilon} + 2)(4\widetilde{\epsilon} - 1)\right], \tag{C.7d}$$

$$d_{N_{I_1}} = 2\Pi(\widetilde{\sigma} - \widetilde{\epsilon})\left[(\widetilde{\sigma} + 2)(2\widetilde{\sigma} + 2\widetilde{\epsilon} - 1) + \Pi^2(\widetilde{\epsilon} + 2)(4\widetilde{\epsilon} - 1)\right], \tag{C.7e}$$

$$d_{N_{I_2}} = Ca_\omega\lambda_2(\widetilde{\sigma} + 2)^2(\widetilde{\sigma}^2 - 2\widetilde{\epsilon} + 1), \tag{C.7f}$$

$$d_{N_{I_3}} = Ca_\omega\lambda_2\Pi^2\left[-5\widetilde{\sigma}^2 + 4\widetilde{\sigma} + 8 + 6\widetilde{\epsilon}(\widetilde{\sigma}^2 + 2\widetilde{\sigma} - 2) + (2\widetilde{\sigma}^2 - 4\widetilde{\sigma} - 13)\widetilde{\epsilon}^2 + 2\widetilde{\epsilon}^3\right], \tag{C.7g}$$

$$d_{N_{I_4}} = Ca_\omega\lambda_2\Pi^4(\widetilde{\epsilon}^2 + \widetilde{\epsilon} - 2)^2. \tag{C.7h}$$

References

1. Q. Wang, Z. Suo, X. Zhao, Nat. Commun. **3**, 1157 (2012).
2. J.S. Eow, M. Ghadiri, Chem. Eng. J. **85**, 357 (2002).
3. H. Kim, D. Luo, D. Link, D.A. Weitz, M. Marquez, Z. Cheng, Appl. Phys. Lett. **91**, 133106 (2007).
4. G. Taylor, Proc. R. Soc. A **291**, 159 (1966).
5. C. Smith, J. Melcher, Phys. Fluids **10**, 2315 (1967).
6. J.R. Melcher, G.I. Taylor, Annu. Rev. Fluid Mech. **1**, 111 (1969).
7. D.A. Saville, Annu. Rev. Fluid Mech. **29**, 27 (1997).
8. S. Torza, R.G. Cox, S.G. Mason, Philos. Trans. R. Soc. A **269**, 295 (1971).
9. O. Vizika, D. Saville, J. Fluid Mech. **239**, 1 (1992).
10. J. Baygents, N. Rivette, H. Stone, J. Fluid Mech. **368**, 359 (1998).
11. R. Allan, S. Mason, Proc. R. Soc. London A: Math. Phys. Eng. Sci. **267**, 45 (1962).
12. C. Sozou, Proc. R. Soc. London A: Math. Phys. Eng. Sci. **331**, 263 (1972).
13. R. Thaokar, Eur. Phys. J. E **35**, 76 (2012).
14. T. Ward, G. Homsy, Phys. Fluids **13**, 3521 (2001).
15. S. Lee, D. Im, I. Kang, Phys. Fluids **12**, 1899 (2000).
16. T. Ward, G. Homsy, J. Fluid Mech. **547**, 215 (2006).
17. C. Christov, G. Homsy, Phys. Fluids **21**, 083102 (2009).
18. N. Kaji, Y. Mori, Y. Tochitani, J. Heat Transfer **107**, 788 (1985).
19. A. Esmaeeli, M.A. Halim, Acta Mech. **229**, 3943 (2018).
20. G. Taylor, Proc. R. Soc. Lond. A **313**, 453 (1969).
21. A. Castellanos, A. Gonzalez, IEEE Trans. Dielectr. Electr. Insul. **5**, 334 (1998).
22. J.Q. Feng, Proc. R. Soc. Lond. A **455**, 2245 (1999).
23. M.N. Reddy, A. Esmaeeli, Int. J. Multiphase Flow **35**, 1051 (2009).
24. A. Esmaeeli, P. Sharifi, J. Electrost. **69**, 504 (2011).
25. T.B. Jones, *Electromechanics of Particles* (Cambridge University Press, New York, USA, 1995).
26. J. Sherwood, J. Fluid Mech. **188**, 133 (1988).
27. T. Tsukada, T. Katayama, Y. Ito, M. Hozawa, J. Chem. Eng. Jpn. **26**, 698 (1993).
28. J.Q. Feng, T.C. Scott, J. Fluid Mech. **311**, 289 (1996).
29. E. Lac, G.M. Homsy, J. Fluid Mech. **590**, 239 (2007).
30. O. Ajayi, Proc. R. Soc. Lond. A **364**, 499 (1978).
31. J.W. Ha, S.M. Yang, J. Fluid Mech. **405**, 131 (2000).
32. A. Esmaeeli, A. Behjatian, Phys. Rev. E **86**, 036310 (2012).